LUDWIG-MAXIMILIANS-UNIVERSITY MUNICH
TECHNICAL UNIVERSITY MUNICH

Master Thesis in Theoretical and Mathematical Physics
submitted by

KIANUSCH VAHID YOUSEFNIA

born in Freiburg im Breisgau (Germany)

JULY 2021

BAYESIAN APPROACH TO LONG-RANGE CORRELATIONS AND MULTIPLICITY FLUCTUATIONS IN NUCLEUS-NUCLEUS COLLISIONS

KIANUSCH VAHID YOUSEFNIA

This Master Thesis has been carried out at the
Institut de Physique Théorique (IPhT), Gif-sur-Yvette, France
under the supervision of
Prof. Dr. Jean-Yves Ollitrault
Second Referee:
Prof. Dr. Nora Brambilla

Kianusch Vahid Yousefnia: *Bayesian approach to long-range correlations and multiplicity fluctuations in nucleus-nucleus collisions,* © July 2021

ABSTRACT

The number of particles detected in a nucleus-nucleus collision strongly depends on the impact parameter of the collision. Therefore, multiplicity fluctuations, as well as rapidity correlations of multiplicities, are dominated by impact parameter fluctuations. We present a method based on Bayesian inference which allows for a robust reconstruction of fluctuations and correlations at fixed impact parameter. We apply the method to ATLAS data on the distribution of charged multiplicity and transverse energy. We argue that multiplicity fluctuations are smaller at large rapidity than around central rapidity. Finally, we suggest simple new analyses in order to confirm this effect.

ZUSAMMENFASSUNG

Die Zahl von Teilchen, die in einer Nukleus-Nukleus-Kollision detektiert werden, hängt stark mit dem Stoßparameter der Kollision zusammen. Aus diesem Grund werden sowohl Multiplizitätsfluktuationen as auch Rapiditätskorrelationen von Multiplizitäten von Stoßparameterfluktuationen überschattet. Wir präsentieren eine Methode, die auf Bayes'scher Inferenz basiert und eine robuste Rekonstruktion von Fluktuationen und Korrelationen bei festem Stoßparameter erlaubt. Wir wenden die Methode auf Daten einer ATLAS-Messung an, bei der die Multiplizität von geladenen Teilchen und die transversale Energie gemessen worden sind. Wir legen dar, dass Multiplizitätsfluktuationen bei großen Rapiditäten kleiner als bei zentralen Rapiditäten sind. Schließlich schlagen wir einfache neue Analysen vor, um diesen Effekt zu bestätigen.

ACKNOWLEDGMENTS

First and foremost I would like to express my gratitude towards my thesis supervisor, Jean-Yves Ollitrault, for his constant support throughout all these months, even at midnight or on a Sunday, for enduring my desperate need to speak with him in French and for making my internship at the IPhT possible in spite of a global pandemic. I would like to thank as well Laure Sauboy for helping me to fill out the "convention de stage" and Laurent Sengmanivanh for installing TRENTo 3D on the cluster of the IPhT.

Thank you also to the Manager of the TMP program, Robert Helling, for financing my travelling between Munich and Paris with TMP funds.

Special thanks go to my eleven housemates. Without them the countless lockdowns would have been unbearable. Lastly, I would like to thank my family for always supporting me no matter what.

CONTENTS

1

INTRODUCTION

Many physicists when asked to brainstorm about the *Large Hadron Collider* think of proton-proton collisions, the discovery of the Higgs boson or the search for physics beyond the Standard Model. However, only few of them think of ultrarelativistic heavy-ion collisions, even though these are arguably at least just as exciting. Beams of nuclei are focussed and collided at energies considerably higher than the rest mass of the nucleus constituents, such that thousands of new particles are produced per nucleus-nucleus collision [1, 2]. The energy is in fact so high that matter becomes about twenty times as dense as a hadron during the collision [3]. As a consequence, the elementary particles making up a nucleon strongly couple to each other, forming a collective medium governed by the laws of strong interaction [2].

Heavy-ion collisions require new concepts not needed in the description of proton-proton collisions. The most prominent one concerns the collision centrality. Physics will be different when the two nuclei collide head-on, which is referred to as a central collision, as opposed to the case in which they barely scratch each other. The underlying geometric quantity is called the impact parameter of a collision and is neither directly measurable in experiments, nor can it be controlled for a given collision. Instead, workers measure proxies of it, e.g. the number of hadrons produced and falling into a specific detector acceptance, so-called hadron multiplicities [4]. Alternatively, one could measure the energy deposit into a calorimeter [5].

Particle production can be measured for different angular sectors simultaneously using multiple detectors positioned at different polar angles, which correspond to different so-called (pseudo)rapidities. In this work, we study fluctuations and correlations between particle production at different rapidities. The measurement of this rapidity-rapidity correlation has remained elusive so far because it is hidden by correlations induced by the variation of the impact parameter, since a more central collision produces more particles at all rapidities. Methods have been proposed to overcome this limitation [6], but in practice, one has been restricted to forward-backward correlation techniques [7–9], in which two detectors are positioned at symmetric bins in pseudorapidity and which are less sensitive to impact parameter fluctuations.

We introduce a simple Bayesian method that allows us to reconstruct correlations at fixed impact parameter b, therefore eliminating the contribution to correlations due to variations of b. More specifically, if $(N_1, ..., N_p)$ denote centrality observables, like multiplicity or energy deposit, in p rapidity windows, we show that their $p \times p$ covariance matrix can be reconstructed for $b = 0$, while a $(p-1) \times (p-1)$ projection of this matrix can be reconstructed for $b > 0$. Bayesian methods in the field of heavy-ion collisions usually involve sophisticated models and extensive calculations [10–12]. In contrast, the Bayesian approach in this work is quite simple, and we do not need to resort to any model of collision dynamics.

We apply the reconstruction to data measured by the ATLAS collaboration. They measured the joint distribution of $(E_T, N_{\rm ch})$, where E_T denotes the total transverse energy measured in a calorimeter located at a large rapidity, and $N_{\rm ch}$ refers to the multiplicity of charged particles measured in the central rapidity region. We will have a lot more to say later on how these observables are defined and what the rapidity specifications mean exactly; for now, it suffices to know they are two centrality observables covering separate detector windows. The histogram of $(E_T, N_{\rm ch})$ for collisions of lead (Pb) nuclei is represented in Fig. 1.1. As the impact parameter of a Pb+Pb collision is not measured, this histogram constitutes the superposition of contributions at all impact parameters. However, we are able to reconstruct accurately the location of central collisions on this diagram, which is represented in the figure as a black curve containing 99 % of all collisions at $b = 0$. This is a specific example of what can be achieved through our Bayesian reconstruction method.

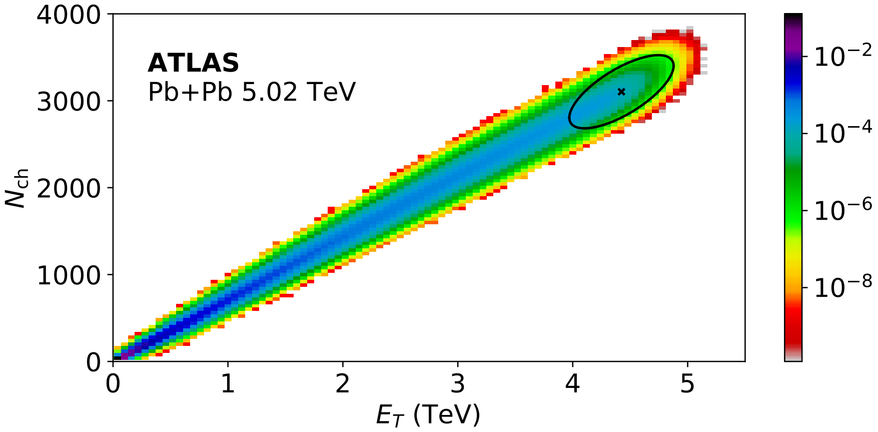

Figure 1.1: Normalized histogram of the distribution of $(E_T, N_{\rm ch})$ measured by the ATLAS collaboration [13] in Pb+Pb collisions at $\sqrt{s_{\rm NN}} = 5.02$ TeV. E_T denotes the transverse energy in the pseudorapidity window $3.2 < |\eta| < 4.9$ and $N_{\rm ch}$ the number of reconstructed tracks of charged particles in the pseudorapidity window $|\eta| < 2.5$. The black ellipse is one of the results obtained through our Bayesian reconstruction, corresponding to the 99% confidence ellipse for collisions at zero impact parameter.

This work is structured in two parts. In Part i we provide the reader with an introduction to the topic of ultrarelativistic heavy-ion collisions, with a focus on those concepts and phenomena needed to understand this work. Part ii represents the main part of this work. We explain our Bayesian method in Chapter 6. It is validated in Chapter 7 using a realistic model calculation in which the impact parameter is known. In Chapter 8, we apply it to ATLAS data. In Chapter 9, we present our results for the fluctuations of E_T and N_{ch} and discuss what they tell us about the early collision dynamics. Finally, in Chapter 10, we suggest analyses that could be done easily with existing data and which would shed light on the rapidity dependence of fluctuations and on long-range correlations.

Part I

ULTRARELATIVISTIC HEAVY-ION COLLISIONS IN A NUTSHELL

2

HOW TO SET UP A COLLISION AND WHY

This chapter aims at providing a gentle introduction to the field of ultrarelativistic heavy-ion collisions. In Section 2.1, we introduce the reader to important vocabulary before presenting the two most important collider facilities as well as a useful coordinate system to describe emitted hadrons. Ultrarelativistic heavy-ion experiments are mainly performed in order to produce and study the properties of a specific collective medium. In Section 2.2, we therefore present some characteristics of this medium and shed light on its space-time evolution during a heavy-ion collision.

2.1 TERMINOLOGY, COLLIDERS AND COORDINATE SYSTEMS

Let us begin by introducing some important vocabulary. A *nucleus-nucleus (A+B) collision* denotes a collision involving two nuclei (A) and (B) made up of more than one nucleon, which makes it different from *proton-nucleus (p+A) collisions* or *proton-proton (p+p) collisions*. Similarly, a *heavy-ion collision* refers to the collision of two "heavy" nuclei – as opposed to collisions of "light" nuclei, protons or even electrons. There seems to be no clear consensus on how many nucleons a nucleus needs to have in order to count as heavy, but typical examples of heavy ions used in experiments include ^{197}Au (gold), ^{208}Pb (lead) and ^{238}U (uranium). In this work, we focus on Pb+Pb collisions only, so that we tend to treat 'nucleus-nucleus collisions' and 'heavy-ion collisions' as synonyms, even though, strictly speaking, they are not. Collisions are further called *ultrarelativistic* if the energy of the nucleons that make up the colliding nuclei is much higher than the nucleon rest energy. Whenever we refer to collisions in this work, we implicitly mean ultrarelativistic ones.

In an experiment, one does not accelerate two nuclei only and makes them collide. Instead, one collides bunches of nuclei, and when two bunches collide, there are multiple nucleus-nucleus collisions, or *events*. The collision energy is typically given in terms of the total energy per nucleon-nucleon pair in the center-of-mass frame, $\sqrt{s_{\mathrm{NN}}}$.

Next, we introduce the collider facilities that are able to perform heavy-ion collisions at ultrarelativistic energies. We will focus on the two colliders with the highest center-of-mass energy, RHIC and the LHC. Both of them are *synchrotron* colliders, meaning they are circular with two beams of nuclei running in opposite directions with an ever increasing magnetic field bending their paths until one makes them cross at the *interaction point*. An aerial view of the two collider facilities is provided in Fig. 2.1.

The Relativistic Heavy Ion Collider (RHIC) is a synchrotron collider located at the Brookhaven National Laboratory (BNL) in Upton, New York, with a storage ring radius of about 610 m. RHIC is fully dedicated to heavy-ion research and has at the moment only one active experiment, STAR, while a second one, PHENIX, is being upgraded. The center-of-mass energies reached are $\sqrt{s_{\mathrm{NN}}} = 500\,\mathrm{GeV}$ for p-p collisions and $\sqrt{s_{\mathrm{NN}}} = 200\,\mathrm{GeV}$ for nucleus-nucleus collisions.

The Large Hadron Collider (LHC), on the other hand, with a radius of 4.3 km constitutes the largest synchrotron and also the largest particle accelerator in the world. It is operated by the European Organization for Nuclear Research (CERN) and performs p-p collisions at 13 TeV and Pb-Pb collisions at $\sqrt{s_{\mathrm{NN}}} = 5.02\,\mathrm{TeV}$. In contrast to RHIC, only for about one month per year are the collision runs devoted to heavy-ion research, while the rest of the time is invested for precision tests of the Standard Model. There are four running collaborations at the LHC, only one of which, ALICE, is fully dedicated to heavy ions. Furthermore, there are subgroups within the collaborations ATLAS and CMS doing heavy-ion research.

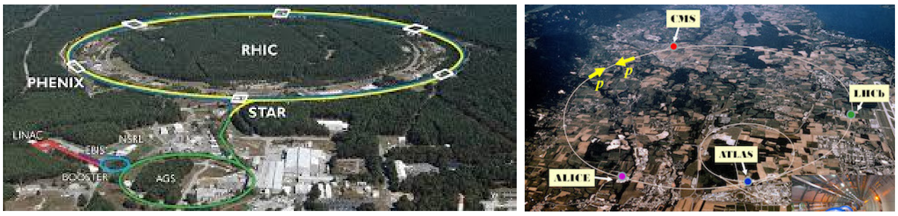

Figure 2.1: Aerial view of the two collider facilities with the highest center-of mass energy. *Left:* Relativistic Heavy Ion Collider (RHIC) at BNL, Upton, New York, USA. *Right:* Large Hadron Collider (LHC) at CERN, Geneva, Switzerland.

In the remainder of this section, we introduce useful coordinates to characterize the hadron output of collisions. The position space coordinate system constitutes a right-handed system of the coordinates (x, y, z), in which we align the z-axis along the beam axis and let the x-axis point to the center of the (circular) collider. The plane (x, y) orthogonal to the beam axis is referred to as the *transverse plane* and, in this spirit, the component of the 3-momentum of a particle in this plane is called *transverse* momentum $\mathbf{p}_t$. The sum of transverse momenta of all particles in a collision event is a conserved quantity, and is in fact zero in the lab frame.

One can alternatively switch to spherical coordinates, in which symmetries of the collision geometry are more visible. For this purpose, let us introduce an azimuthal angle ϕ in the transverse plane and a polar angle θ (see Fig. 2.2). However, we will directly replace θ with the *pseudorapidity* η defined by:

$$\eta \equiv -\log\tan(\theta/2) = \frac{1}{2}\log\frac{|\mathbf{p}| + p_z}{|\mathbf{p}| - p_z} \tag{2.1}$$

With this definition, particle emission at $\eta = 0$ is within the transverse plane ($\theta = \pi/2$), while emission along the beam axis corresponds to $\eta = \pm\infty$. This variable transformation is actually motivated by Lorentz invariance. To see this, note first that the pseudorapidity relates to the longitudinal component p_z of momentum thusly:

$$p_z = p_t \sinh(\eta). \tag{2.2}$$

When p_t is much larger than the particle mass m, which is usually a reasonable assumption in the ultrarelativistic regime, then η is to a good approximation equal to the *rapidity* y, defined through the relation

$$p_z = \sqrt{p_t^2 + m^2}\sinh(y), \tag{2.3}$$

where we use units in which the speed of light is set to 1. The rapidity y has the interesting property that it is additive under Lorentz boosts, which is then inherited to the pseudorapidity η in ultrarelativistic nucleus-nucleus collisions. This means that differences between pseudorapidities are approximately Lorentz-invariant. We will allow ourselves from time to time to call η simply *rapidity* instead of pseudorapidity. There is also a third quantity involving the time coordinate t called *spacetime rapidity*,

$$\eta_s \equiv \frac{1}{2}\log\frac{t+z}{t-z}. \tag{2.4}$$

If one assumes that the produced particles are massless and free-streaming in the z-direction, then $z/t = p_z/|\mathbf{p}|$, such that $\eta_s \simeq \eta$.

Particle emission around $\eta = 0$ ($\theta = \pi/2$) is referred to as emission around *midrapidity*. Accordingly, detectors covering the hemisphere $\eta > 0$ ($\theta < \pi/2$) detect particle emission at *forward rapidity*, while *backward rapidity* corresponds to $\eta < 0$ ($\theta > \pi/2$).

Furthermore, an emitted particle with mass m and transverse momentum $\mathbf{p}_t$ has a *transverse mass*,

$$m_t \equiv \sqrt{\mathbf{p}_t^2 + m^2}, \tag{2.5}$$

as well as a *transverse energy*,

$$E_t \equiv E\sin\theta = \frac{E}{\cosh\eta}, \tag{2.6}$$

where $E = \sqrt{\mathbf{p}^2 + m^2}$ denotes the total energy of the particle. Calorimeters measure the total transverse energy $E_T \equiv \sum E_t$ of hadrons falling into the detector acceptance.

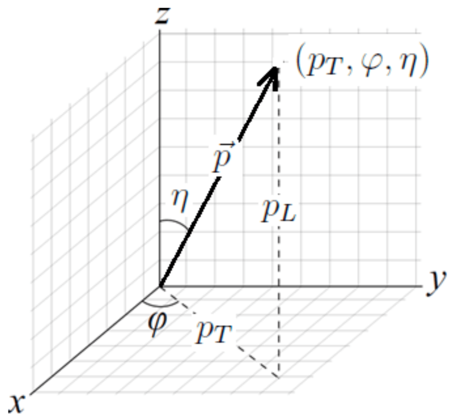

Figure 2.2: Coordinate system to represent the 3-momentum vector **p** of a particle produced in a heavy-ion collision. The polar angle θ has been traded for the pseudorapidity η.

2.2 QUARK-GLUON PLASMA

On February 10, 2000, a CERN press release reports "compelling evidence for the existence of a new state of matter in which quarks (...) are liberated to roam freely."[1] What has been announced that day has since then been dubbed *quark-gluon plasma (QGP)*, a locally thermalized, strongly interacting state of matter in which quarks and gluons move freely over distances large in comparison to the typical size of a hadron [2]. In order to produce QGP in a laboratory, heavy ions have to be collided at ultrarelativistic energies. The study of the bulk properties of QGP is actually the primary reason to perform ultrarelativistic heavy-ion collisions.

In recent years, it has been understood that QGP, while being governed by the laws of quantum chromodynamics (QCD), behaves collectively like an almost ideal relativistic hydrodynamic fluid, which offers the interesting possibility to study the relationship between microscopic properties described by QCD and macroscopic quantum field quantities like densities of energy or entropy.

The subsequent paragraphs aim at providing an end-to-end description of the heavy-ion collision process and how QGP relates to it. A thorough review is given in [3]. Let us turn to Fig. 2.3, which presents schematically the most prominent phases of the collision evolution. Note that the figure provides a time variable τ alongside it. Actually, τ denotes the *proper time* defined by

$$\tau = \sqrt{t^2 - z^2}, \tag{2.7}$$

where t denotes the time coordinate in the laboratory frame such that $t = 0$ at the time of the interaction of the two nuclei. But since the time

---

[1] `https://home.cern/news/press-release/cern/new-state-matter-created-cern`, last visit: July 29, 2021

values are meant to give rough estimates only, the difference between t and τ is not too important for our purposes.

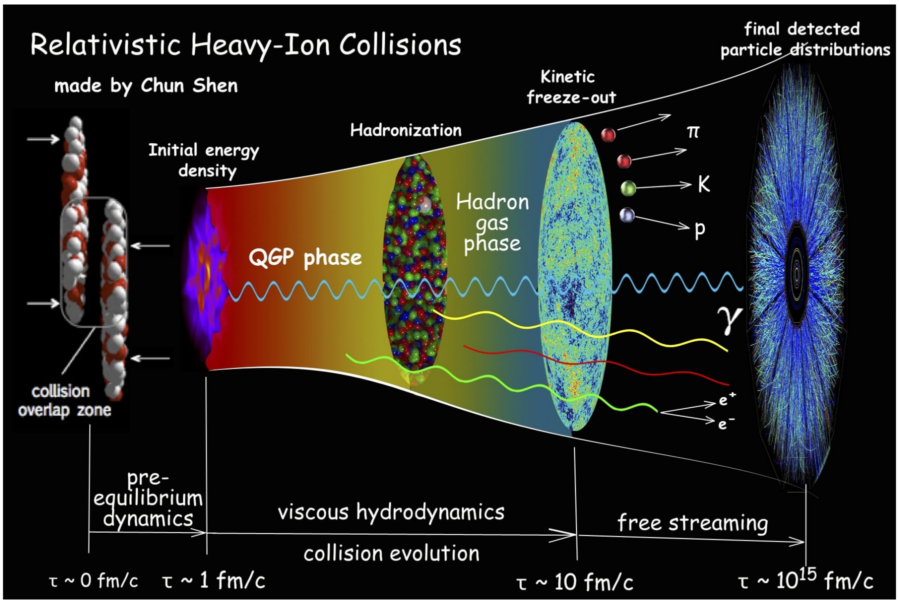

Figure 2.3: Sketch of a ultrarelativistic heavy-ion collision evolution by Chun Shen.[2]

So consider two heavy nuclei that approach each other along the beam axis. Due to the ultrarelativistic regime, the nuclei are Lorentz-contracted to flat discs. At $t = 0$, the nuclei interact with each other and also cross one another. The corresponding point in space is also referred to as *interaction point*. The system is at this moment out of thermal equilibrium; it takes about 1 fm/c for it to thermalize. What we obtain is a lumpy distribution of energy density in the transverse plane which looks different from one collision event to another because of the quantum fluctuations of the nuclear constituents. In Chapter 4 we offer a description of how to model initial field profiles mathematically.

Once thermalized, the system has undergone the phase transition towards QGP. During LHC experiments, the energy density of this extremely dense state of matter is at this stage twenty times as high as that of a hadron [3]. Since the produced QGP is so dense and hot, workers like to refer to it as *fireball*. The fireball enters a process of expanding and cooling down, which, remarkably, can be described in terms of fluid degrees of freedom using relativistic viscous hydrodynamics. A recent numerical scheme for solving the relativistic fluid equations of motion is described in [14].

Once the droplet of QGP has cooled down sufficiently, to a temperature of around 150 MeV, it converts into a hadron gas, with unstable hadrons initiating a cascade into stable particles. Once there are no inelastic processes, the system has undergone what is called *chemi-*

---

[2] `https://u.osu.edu/vishnu/category/visualization/`, last visit: July 29, 2021

cal freeze-out. There are still elastic interactions; only once the *kinetic freeze-out* has occured do the particles move freely.

The last stage of the collision after the kinetic freeze-out is referred to as *free streaming*. Thousands of new particles that have emerged from the collision of the two incident nuclei stream to the detector. It is from particle distributions and correlations that one aims at deducing properties of QGP.

The important fact to remember is that QGP appears during an intermediate stage of a heavy-ion collision. What is experimentally accessible, however, is the final state of the evolution only, for instance hadron spectra. The fact that those result from an integrated history of time evolution during which fluctuations in the initial fields can be intensified or attenuated is what makes the study of QGP properties so challenging. An additional complication arises from the fact that the initial conditions and their symmetry properties depend on the collision centrality, i.e. whether the two nuclei collide head-on or in a peripheral manner. The underlying geometric quantity, the impact parameter, is not directly measurable either. Chapter 3 focuses on the concept of centrality in detail.

3

THE CONCEPT OF EVENT CENTRALITY

In this chapter we will introduce a key concept needed for this work, namely *collision centrality*. It is motivated by the fact that, in heavy-ion physics, observed phenomena critically depend on the initial geometry of the collision. In simple terms, it makes a huge difference whether two nuclei collide head-on or barely scrape each other.

Let us consider two nuclei approaching each other along the beam axis. Their centers projected onto the transverse plane define the vector **b**, the modulus of which is called the *impact parameter* of the collision. The impact parameter is the natural variable to characterize the initial geometry of a collision event. The definition of b is schematically illustrated in Fig. 3.1.

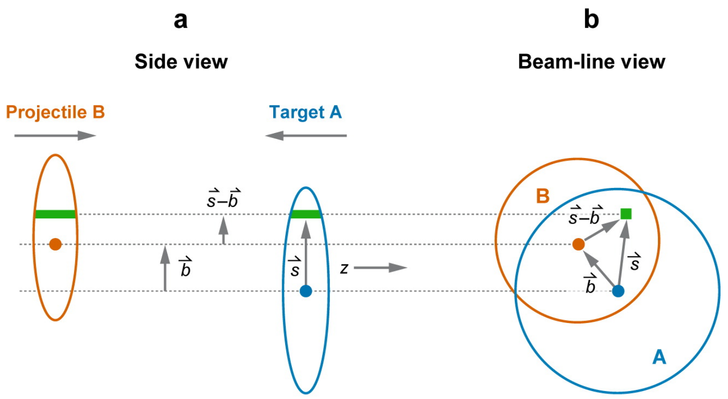

Miller ML, et al. 2007.
Annu. Rev. Nucl. Part. Sci. 57:205–43

Figure 3.1: Schematic representation of the collision geometry, both in side view *(left)* and in beam-line view *(right)*. Dashed lines connect the positions of various structures in the two perspectives. The impact parameter vector **b** connects the two nucleus centers in the transverse plane while **s** denotes an arbitrary two-dimensional vector in the transverse plane. Figure taken from [15, fig. 3].

When colliding heavy ions in an experiment, one obtains events at all impact parameters. We are typically dealing with what are called *minimum-bias* events. This means that there is no selection of events in terms of b. When measuring some final state observable in an experiment, one is interested in averaging the results of many events. But since final state observables will depend on the impact parameter, this averaging is sensible only if the events one averages over have similar impact parameters, say e.g. $1\,\text{fm} \leq b \leq 1.5\,\text{fm}$.

This is formalized through the concept of centrality classes. In order to understand this, we will first introduce $P_{\text{inel}}(b)$, which is the probability for an inelastic nucleus-nucleus interaction to occur at a given impact parameter. Its typical form is given on the left-hand side of Fig. 3.2: P_{inel} is basically equal to unity up to impact parameters twice the radius R_A of the colliding nuclei, meaning that when the nuclei are sufficiently close to each other that they geometrically pass through each other, an inelastic collision will take place. On the other hand, P_{inel} quickly falls off when $b > 2R_A$. The figure results from a model calculation that will be introduced in more detail in Section 4.2.

Using this quantity, one can write down the differential inelastic nucleus-nucleus cross section:

$$\frac{d\sigma}{db}(b) = P_{\text{inel}}(b) 2\pi b. \tag{3.1}$$

Integrating over all impact parameters yields the total inelastic nucleus-nucleus cross section σ_{inel}. On the right-hand side of Fig. 3.2, we present the differential cross section divided by the total cross section of inelastic nucleus-nucleus interactions. This is nothing but the normalized probability distribution of impact parameters for minimum-bias collisions. It increases linearly until $b \simeq 2R_A$ and then drops to zero.

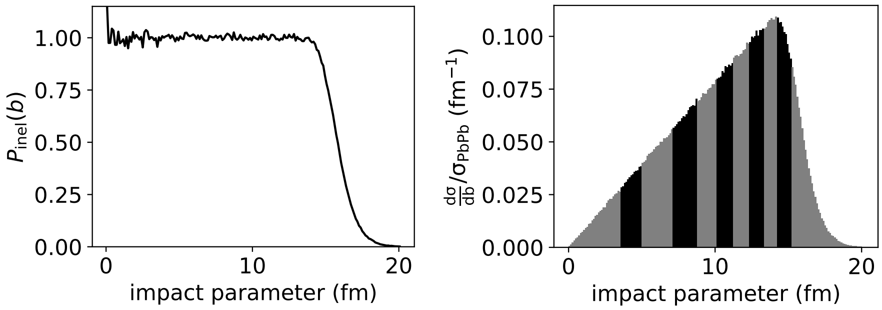

Figure 3.2: *Left:* Probability for an inelastic collision to occur at a given impact parameter. *Right:* Normalized probability distribution of b, which is given by the differential inelastic cross section divided by the total inelastic nucleus-nucleus cross section. It further contains, from left to right, the centrality classes 0-5 %, 5-10 %, 10-20 %, ..., 90-100 % based on the impact parameter, see text for details. Both figures have been obtained by simulating and binning $1.2 \cdot 10^6$ minimum-bias Pb+Pb collisions at $\sqrt{s_{\text{NN}}} = 5.02\,\text{TeV}$ using the TRENTo 3D initial condition model (see Section 4.2 for details.)

Now we are ready to introduce the *b-centrality* of a collision at impact parameter b as the cumulative probability distribution of impact parameters:

$$c_b(b) = \frac{1}{\sigma_{\text{inel}}} \int_0^b P_{\text{inel}}(b') 2\pi b' \, db' \tag{3.2}$$

Note that for impact parameters $b < 2R_A$, the probability P_{inel} is essentially constant and equal to unity, which is why the integral in Eq. (3.2) can be performed straightforwardly:

$$c_b(b) = \frac{\pi b^2}{\sigma_{\text{inel}}} \qquad \text{for } b < 2R_A \tag{3.3}$$

We can now introduce *centrality classes* based on b-centrality. For example, one can define the 0-5 % class, which contains those 5 % of all minimum-bias events with the lowest impact parameter, or equivalently, events with $0 < c_b < 0.05$. Similarly, the 5-10 % class contains events with $0.05 < c_b < 0.10$, and so on. We illustrate some centrality intervals in the right panel of Fig. 3.2. Note that it is common usage to characterize the centrality edges in terms of percentiles. Furthermore, centrality intervals do not always have a size of 5 %.

At this point, some vocabulary is in order. Collisions with a low impact parameter are called *central* collisions, in contrast to *peripheral* collisions. On the other hand, there do not seem to be sharply defined limits in terms of centrality. Sometimes workers even use the term *most central* / *ultracentral* for collisions at impact parameters close to zero. Similarly, *mid-central* collisions refer to events with ∼ 20-40 % centrality.

The concept of b-centrality provides a straightforward way of categorizing events as a function of the impact parameter, and is a natural way of defining centrality from a theoretical point of view. It is, however, impractical for the classification of *actual* collision events measured using detectors because one would have to know the impact parameter of every single collision, and the impact parameter is *not* directly measurable.

What is done in experiments, instead, is to resort to "proxies" for the impact parameter, e.g. the number of particles produced in an event (event *multiplicity*) or the amount of energy deposited in a calorimeter. Put simply, we expect more particles to be produced when the nuclei collide head-on (central collisions) as opposed to when they scratch each other (peripheral collisions). Here are some examples of experimental observables used by the collaborations introduced in Section 2.1:

- STAR [16]: number of tracks of charged particles detected in the pseudorapidity window $-0.5 < \eta < 0.5$
- ALICE [4]: number of hits in two scintillators covering the windows $-3.7 < \eta < -1.7$ and $2.8 < \eta < 5.1$
- ATLAS [13]: energy deposited in two forward calorimeters covering $3.2 < |\eta| < 4.9$
- CMS [5]: energy deposited in two forward calorimeters covering $3.0 < |\eta| < 5.2$

Given an observable n and its probability distribution $P(n)$, one can define an experimental measure of centrality that we will denote by c:

$$c(n) = \int_{n}^{\infty} P(n)\,\mathrm{d}n \tag{3.4}$$

Note that n appears as a lower bound in the integral, in contrast to the definition of b-centrality. This is because centrality observables are monotonously decreasing functions of the impact parameter. With this definition of centrality, one can define centrality classes in the very same fashion as for b-centrality, with the 0-5 % class this time corresponding to events with the highest values of n. In general, collisions at fixed impact parameter display a distribution of n, and vice versa. For large collision systems like Pb-Pb, however, there is a tight correlation between c_b and c, such that it is a reasonable assumption in most cases that centrality classes in b and centrality classes in n essentially describe the same set of events. Only for ultracentral collisions, when $c \sim 1\,\%$, does one observe deviations, such that the influence of finite fluctuations of n at fixed b becomes relevant [17].

4

DESCRIBING THE INITIAL CONDITIONS OF HEAVY-ION COLLISIONS

This chapter is devoted to describing how the initial field density of energy or entropy can be modeled. On the one hand, these initial conditions are needed as input to hydrodynamic simulations of QGP, which is beyond the scope of this work. On the other hand, it is commonly agreed that multiplicity fluctuations, while certainly affected by QGP evolution, originate in the early collision dynamics [15]. This means that we can study multiplicity fluctuations without resorting to extensive hydrodynamic simulations and instead look at the initial conditions.

A large class of initial condition models is based on Glauber theory. These models consider a nucleus-nucleus collions as a superposition of independent nucleon-nucleon collisions and promote the number of nucleons "participating" in the collision and the number of binary nucleon-nucleon collisions to relevant quantities. Initial event distributions are then sampled according to the position of theses variables. A review of Glauber modeling is given in [15]. After thoroughly highlighting the main aspects of Glauber theory relevant for this work in Section 4.1, we will, in Section 4.2, give an overview of the TRENTo 3D model of initial conditions, which uses a similar ansatz and is our initial condition model of choice later on.

4.1 THE GLAUBER MODEL

In order to understand the purpose of the Glauber model, let us look at Fig. 4.1. On the left, it shows two Lorentz-contracted nuclei that are about to collide with impact parameter **b**. Now, what the Glauber model does is to introduce the concept of *participants*, i.e. nucleons that participate in the collision. Those are depicted schematically in color on the right-hand side of Fig. 4.1. On the other hand, those nucleons that do not partake are referred to as *spectators*. Another important quantity is the number of binary nucleon-nucleon collisions N_{coll} in an event. The Glauber model allows to express the number of participants N_{part} and N_{coll} as a function of the impact parameter and how these quantities can be related to experimental data like multiplicity distributions.

Over the years, two strategies have been established: The first of them is called *optical limit approximation* and constitutes a framework of continuous nucleon density distributions used to make the full quantum-mechanical scattering integral numerically tractable [15].

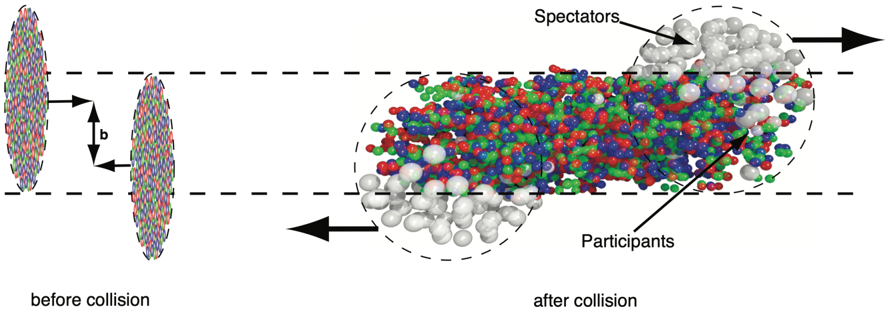

Figure 4.1: Two nuclei collide with impact parameter **b**. The participating nuclei (in color) are those that interact during the collision while the spectators (in grey) remain unaffected. Figure taken from [18, fig. 1]

The other one consists of sampling nucleons "from scratch" on a computer, which is known as the *Glauber Monte Carlo* approach. It is the latter strategy of *event-by-event* calculations that has been found to be easily generalizable to more realistic particle production codes like the TRENTo model, which is why in this work we will consider the Glauber Monte Carlo approach only. In any case, as far as the calculation of N_{part} and N_{coll} is concerned, the two strategies lead to essentially identical results [15].

In order to build nucleus-nucleus collision events in the Glauber Monte Carlo model, one starts by sampling the positions of nucleons, which make up the two nuclei. Specifically, one assumes that these positions are drawn independently from each other from the same probability distribution. The distribution of choice for heavy nuclei is the Woods-Saxon profile of nuclear charge density:

$$\rho(r) = \rho_0 \frac{1 + w(r/R)^2}{1 + \exp\left((r - R)/a\right)} \tag{4.1}$$

There are four parameters in this parametrization: R characterizes the nuclear radius and a the *skin depth* of the nucleus, which corresponds to the length scale over which the density falls off. The parameter w is used to describe nuclei whose maximal density is reached at $r > 0$ ($w = 0$ for Pb). The normalization ρ_0 is chosen such that $\int \mathrm{d}r\, 4\pi r^2 \rho(r) = 1$. Some profiles are given in Fig. 4.2. Note that these parameters are determined independently in low-energy electron-ion scattering experiments [15].

Once the right amount of nucleons have been sampled for the two nuclei, e.g. 2×208 in the case of lead, one draws the impact parameter b of the collision event by sampling from a probability distribution proportional to $2\pi b$, up to a maximum $b_{\mathrm{max}} \approx 20\,\mathrm{fm}$. b_{max} is chosen larger than twice the nuclear radius, just up to the point that the interaction probability (see also Fig. 3.2) drops to zero. Next, the nucleons are collectively shifted by $\pm b/2$ to arrange an impact parameter of b. This begs for a comment. In principle, the

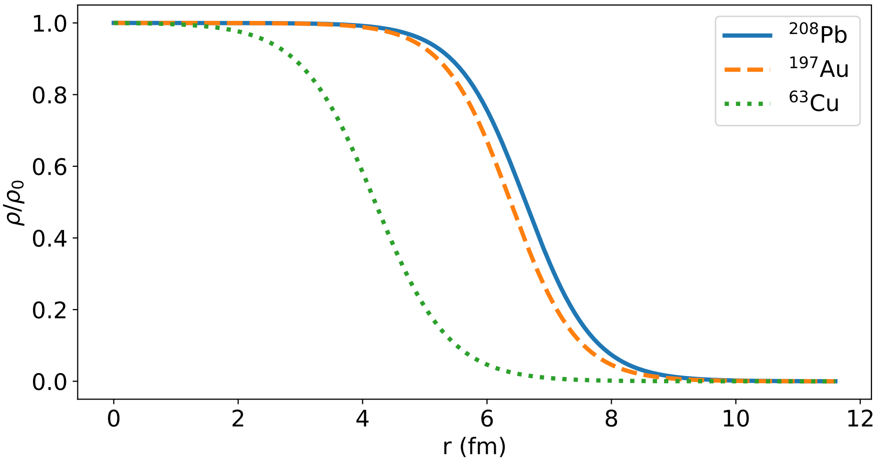

Figure 4.2: Density profiles for ^{208}Pb ($R = 6.624$ fm, $a = 0.549$ fm, $w = 0$), ^{197}Au ($R = 6.38$ fm, $a = 0.535$ fm, $w = 0$) and ^{63}Cu ($R = 4.2$ fm, $a = 0.596$ fm, $w = 0$) according to Eq. (4.1). Parameter values from [19].

impact parameter is a two-component vector in the transverse plane. Its orientation, however, follows a uniform distribution. The plane spanned by the beam axis and the impact parameter vector is called *reaction plane* and has a random orientation in experiments. In initial condition models, it is instead common practice to keep the orientation of the reaction plane fixed, such that the impact parameter vector is aligned with the x-axis (cf. Fig. 4.3), and a single number suffices to characterize it.

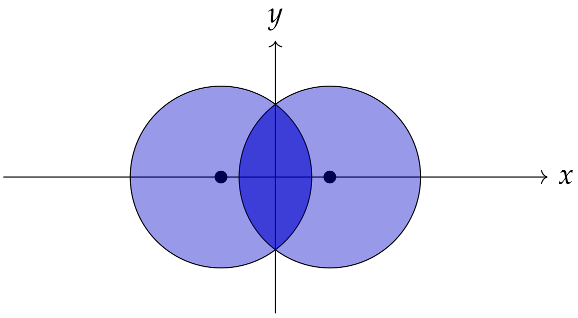

Figure 4.3: Coordinate system in the Glauber model: the x-axis is aligned such that both nucleus centers lie on it. The reaction plane is then spanned by the x-axis and the beam axis, the reaction plane angle is fixed at zero.

Having two nuclei A and B with a displacement b at hand, it is now time to make them collide. For this purpose, we will assume that the nucleons follow straight lines during the collision, from which they are not deviated at any time. In practice, the three-dimensional nucleon positions of both nuclei are projected onto the transverse plane and for each nucleon n of a given nucleus, one checks if there is, within a distance D, at least one nucleon that belongs to the other nucleus. If so, then n is tagged as participant, otherwise as spectator. The distance threshold D is typically parametrized thusly:

$$D = \sqrt{\sigma_{\mathrm{NN}}/\pi} \tag{4.2}$$

Here, σ_{NN} denotes the inelastic nucleon-nucleon cross section. σ_{NN} is measured independently by means of p-p collisions and depends on the collision energy. It is actually through σ_{NN} only that $\sqrt{s_{\mathrm{NN}}}$ enters the Glauber model. Equation (4.2) is motivated by the fact that the de-Broglie wavelength of ultrarelativistic nucleons is small in comparison to their spatial extent. Hence, quantum-mechanical effects are negligible and a black-disk approximation can therefore be expected to constitute a reasonable approximation of the nucleon-nucleon cross section.

Hence, one obtains N_{part} simply by counting the number of participating nucleons in an event. Similarly, one obtains the number of binary collisions N_{coll} by looping over all pairs with one nucleon from nucleus A and the other one from B and counting those nucleon pairs with a separation $d < D$. Note that nucleons can participate in more than one nucleon-nucleon collision. In this case, however, the Glauber model does not account for any loss of nucleon energy, σ_{NN} remains constant for all nucleon-nucleon interactions.

This concludes the description of how $N_{\mathrm{part}}(b)$ and $N_{\mathrm{coll}}(b)$ are computed in the Glauber model. As an application, we sketch how to compute the total nucleus-nucleus cross section σ_{AA} from these quantities. It turns out to be simply a matter of counting, one takes the geometrical cross section with the maximal impact parameter b_{max} introduced in the b-sampling procedure and corrects it by the fraction of events with at least one nucleon-nucleon collision [4]:

$$\sigma_{\mathrm{AA}} = \frac{\#\text{ events with } N_{\mathrm{coll}} \geq 1}{\#\text{ events with } N_{\mathrm{coll}} \geq 0} \times \pi b_{\mathrm{max}}^2 \tag{4.3}$$

4.2 THE TRENTO 3D MODEL OF INITIAL CONDITIONS

Having discussed the Glauber model, we now transition to a more realistic model, namely TRENTo 3D [20], a state-of-the-art Monte Carlo generator of the initial state of proton-nucleus and nucleus-nucleus collisions. In addition to the classical Glauber model, it is also capable of describing the rapidity dependence of initial conditions. TRENTo 3D actually constitutes a generalization of a simpler model, the boost-invariant TRENTo model of initial conditions, which is why we will start with the original model and then discuss how rapidity effects are implemented.

The reduced Thickness Event-by-event Nuclear Topology (TRENTo) initial-condition model [21] generates event-by-event initial transverse entropy density profiles, reproducing the multiplicity distributions for a wide range of LHC experiments. It constitutes a Monte Carlo model that effectively interpolates between previously existing initial condition models. The key quantities are two nucleus thickness functions T_A and T_B. They are modeled as superpositions of Gaussian nucleon densities $\rho_{\text{nucleon}}(\mathbf{x})$ that are centered around previously sampled participating nucleon positions,

$$T_A(\mathbf{x}) = \sum_{i=1}^{N_{\text{part}}} w_A^{(i)} \int \mathrm{d}z \, \rho_{\text{nucleon}}(\mathbf{x} - \mathbf{x}_i), \tag{4.4}$$

and similarly $T_B(\mathbf{x})$. The coordinates $\mathbf{x}_i$ denote the position of participant i. The strength $w_A^{(i)}$ by which a participant contributes is sampled from a Γ-distribution with unit mean,

$$P_k(w) = \frac{k^k}{\Gamma(k)} w^{k-1} \exp(-kw). \tag{4.5}$$

Here, $k > 0$ is a continuous shape parameter regulating the fluctuations. The distribution has a long tail for $k < 1$ while fluctuations are suppressed for $k \gg 1$.

In short, one identifies the participating nucleons for the two given nuclei and deposits a “blob” of entropy at their positions to obtain the two thickness functions of the event.

Next, the TRENTo model assumes the transverse initial entropy density profile to be proportional to the generalized mean of T_A and T_B,

$$s(x, y) = \mathcal{N} \left(\frac{T_A^p + T_B^p}{2} \right)^{1/p}, \tag{4.6}$$

with some normalization constant $\mathcal{N}$. This relation between functions is to be understood pointwise. The dimensionless parameter $p \in \mathbb{R}$ controls the mixing of the two nucleus thickness functions. Note that for $p = 1$, we effectively fall back to the Glauber model since the entropy density is then simply a superposition of Gaussians at the participating nucleon positions. The parameter k in the Γ-distribution can be tuned to match measured multiplicity distributions once p has been chosen.

The TRENTo 3D model now generalizes the original boost-invariant model by adopting a factorized approach for the initial entropy density s:

$$s(\mathbf{x}, \eta) = f(\mathbf{x}) g(\mathbf{x}, \eta_s) \tag{4.7}$$

Here, f denotes the entropy density in the transverse plane at midrapidity computed with the original model, while g is a rapidity-dependent function normalized such that $g(\mathbf{x}, 0) = 1$ for all $\mathbf{x}$ in the transverse plane (η_s denotes spacetime rapidity, cf. Eq. (2.4)). g is defined using a cumulant expansion; it is by adjusting the first three cumulants that the model controls longitudinal entropy deposition. Those have been tuned to reproduce several rapidity-dependent observables. The code for TRENTo 3D is publicly available[1] and returns, for each collision event, an entropy density profile $s(x, y, \eta)$ at an early time after the collision, when hydrodynamics becomes applicable.

---

[1] `https://github.com/Duke-QCD/trento3d`, last visit: July 29, 2021

5

PARTICLE PRODUCTION AND MULTIPLICITY FLUCTUATIONS

Having familiarized ourselves with the most important concepts of heavy-ion collisions with a focus on event centrality and initial conditions, we now consider mechanisms of particle production and how they relate to fluctuations and correlations of final-state centrality observables. A considerable emphasis will be put on discussing different origins of fluctuations.

Particle production in ultrarelativistic nucleus-nucleus collisions can be considered as the statistical emission from a continuous source. Specifically, the source in question is, as we have seen in Section 2.2, a viscous fluid. In numerical codes, the transition from the QGP phase to the hadron gas phase (cf. Fig. 2.3) is implemented as follows [3]: Having introduced a spacetime grid on which the fluid is discretized for the hydrodynamic description, one keeps track of the local temperature of each fluid cell. This temperature keeps decreasing during the QGP expansion and eventually drops below a critical temperature $T_c \approx 150\,\text{GeV}$. At this point a fluid cell converts into hadrons.

A key assumption of hydrodynamic modelling in ultrarelativistic nucleus-nucleus collisions is what has been dubbed *flow paradigm*: Within a collision event, newly produced particles are emitted independently from one another. Put more precisely, the output of a hydrodynamic spacetime simulation of QGP is a *single-particle* momentum distribution, and all particles in a given event are emitted according to this probability distribution [22]. The flow paradigm has been shown to correctly predict several observables of ultrarelativistic nucleus-nucleus collisions, for example *anisotropic flow*. This is a phenomenon according to which initial-state anisotropy in position space, induced by a non-vanishing impact parameter, is transferred by the QGP medium to the final-state azimuthal particle spectra [22, 23].

In this thesis, however, we are not concerned with the azimuthal distribution of particle multiplicity. Instead, we are interested in fluctuations and correlations between centrality observables with a pseudorapidity separation. Henceforth, we define a centrality observable N (like hadron multiplicity, energy deposit) for a given event as the sum of contributions x_i coming from M particles falling into a detector acceptance with a specific pseudorapidity window,

$$N = \sum_{i=1}^{M} x_i. \tag{5.1}$$

Given two (or more) observables N_1, N_2 with disjoint pseudorapidity windows, we distinguish three categories of contributions to their covariance matrix:

1. *Poisson fluctuations:* Even if the contributions x_i in Eq. (5.1) were independent, non-fluctuating variables, there is a contribution to the variance of N stemming from event-by-event fluctuations of the particle multiplicity M. As this contribution does not shed light on the collision dynamics, we estimate it and subtract it from experimental measurements. Assuming M follows a Poisson distribution and $x_i = x$ for all i, then one obtains the following contribution to the variance of N:

   $$\mathrm{Var}(N)_{\mathrm{Poisson}} = \langle M \rangle x^2 \tag{5.2}$$

   Poisson fluctuations only affect variances, there is no contribution to the covariance between N_1 and N_2.

2. *Variation of global variables:* There are further contributions to the covariance matrix that originate from fluctuations of global collision variables like the impact parameter b. If b becomes, say, smaller from one event to another, this will likely increase the the outcome of both measured centrality observables N_1 and N_2. In Chapter 6, we present a method to extract information on correlations of centrality observables at *fixed* impact parameter from the measurement of minimum-bias collisions in order to eliminate contributions from b-fluctuations. A second example of a fluctuating global collision variable is given below.

3. *Dynamical fluctuations:* These are the physically interesting contributions to the covariance matrix, which one aims at isolating. If present, they contain information on whether particle production at different rapidities is correlated.

In the remainder of this chapter, we discuss a simple statistical model of particle production measured through two centrality observables N_1 and N_2 covering different pseudorapidity windows [24, 25]. We assume that a nucleus-nucleus collision at impact parameter b produces N_s sources, each of which contributes to both N_1 and N_2. We further assume that these sources are independent. This can be motivated as follows. The sources are localized in the transverse plane, while the two nuclei are strongly Lorentz-contracted due to the ultrarelativistic regime. For this reason, spatially separated sources are causally disconnected. We denote by $n_i^{(k)}$ the contribution of source k to N_i. The centrality observables of a given event result then as

$$N_i = \sum_{k=1}^{N_s} n_i^{(k)}, \qquad i \in \{1, 2\}. \tag{5.3}$$

In order to obtain quantitative information on the covariance structure of the N_i under these assumptions, we need to formalize these assumptions slightly. Let the contributions n_1 and n_2 of a single source to N_1 and N_2 be sampled from a bivariate probability distribution $p(n_1, n_2)$, while N_s follows a discrete probability distribution $f(N_s)$.

It is now most useful to introduce a *moment-generating function*,

$$\begin{aligned} Z(j_1, j_2) &\equiv \langle \exp(j_1 N_1 + j_2 N_2) \rangle \\ &\equiv \sum_{N_s} f(N_s) \left(\prod_{k=1}^{N_s} \int \mathrm{d}n_1^{(k)} \mathrm{d}n_2^{(k)}\, p\left(n_1^{(k)}, n_2^{(k)}\right) \right) \exp(j_1 N_1 + j_2 N_2), \end{aligned} \tag{5.4}$$

This is a function of two auxiliary variables j_1, j_2 that has the property $Z(0,0) = 1$ and that moments of N_1 and N_2 can be obtained by differentiating with respect to the auxiliary variables:

$$\langle N_1^m N_2^n \rangle = \left. \frac{\partial^{m+n} Z(j_1, j_2)}{\partial j_1^m \partial j_2^n} \right|_{j_1 = j_2 = 0} \tag{5.5}$$

Using Eq. (5.3) and that all sources follow the same probability distribution p, we see that Z factorizes,

$$Z(j_1, j_2) = \sum_{N_s} f(N_s) \left(\int \mathrm{d}n_1 \mathrm{d}n_2\, p(n_1, n_2) \exp(j_1 n_1 + j_2 n_2) \right)^{N_s} . \tag{5.6}$$

We obtain for the means of the centrality observables

$$\langle N_i \rangle = \langle N_s \rangle \langle n_i \rangle, \qquad i \in \{1, 2\}, \tag{5.7}$$

and for the elements $\Sigma_{ij} = \langle N_i N_j \rangle - \langle N_i \rangle \langle N_j \rangle$ of the covariance matrix[1]

$$\Sigma_{ij} = \mathrm{Var}(N_s) \langle n_i \rangle \langle n_j \rangle + \langle N_s \rangle \mathrm{Cov}(n_i, n_j). \tag{5.8}$$

The first term accounts for event-by-event fluctuations the number N_s of sources. This is a second example of a global collision variable inducing correlations, similarly as variations of the impact parameter. Note that even if we consider collisions at a fixed impact parameter, intrinsic fluctuations of N_s are still conceivable. The second term is physically more interesting since it features the covariance matrix of a single source. Since N_1 and N_2 cover different pseudorapidity windows, the second term in Eq. (5.8) sheds light on dynamical rapidity-rapidity correlations.

---

[1] Quantum field theory enthusiasts know that in order to obtain the covariance matrix element Σ_{ab}, there is a shortcut to computing $\langle N_a N_b \rangle$ and subtracting $\langle N_a \rangle \langle N_b \rangle$ from it. It suffices to differentiate the *cumulant-generating function* $\log(Z(j_1, j_2))$ with respect to j_a and j_b and set the auxiliary variables to zero afterwards.

Part II

BAYESIAN APPROACH TO LONG-RANGE CORRELATIONS AND MULTIPLICITY FLUCTUATIONS IN NUCLEUS-NUCLEUS COLLISIONS

6

METHOD

Consider p experimental centrality observables $N_1, ..., N_p$ as introduced in Chapter 3, which cover separate detector windows. Assume further that we are given the joint distribution $P(N_1, ..., N_p)$ measured in a heavy-ion collision experiment. A concrete example is given in Fig. 6.1. The ATLAS collaboration has performed minimum-bias Pb+Pb collisions at $\sqrt{s_{\mathrm{NN}}} = 5.02\,\mathrm{TeV}$ and measured simultaneously two centrality observables for each event,

- the transverse energy E_T in the pseudorapidity window $3.2 < |\eta| < 4.9$ and
- the number N_{ch} of reconstructed tracks of charged particles in the pseudorapidity window $|\eta| < 2.5$.

Our goal is to reconstruct as much information as possible from the distribution in Fig. 6.1 without assuming any specific model of collision dynamics. For this purpose, we introduce momentarily a simple method based on Bayesian inference that has been proven successful for the single-variable case $p = 1$ [26]. In this work, we generalize the approach to the multi-variable case and apply it to ATLAS data with $p = 2$.

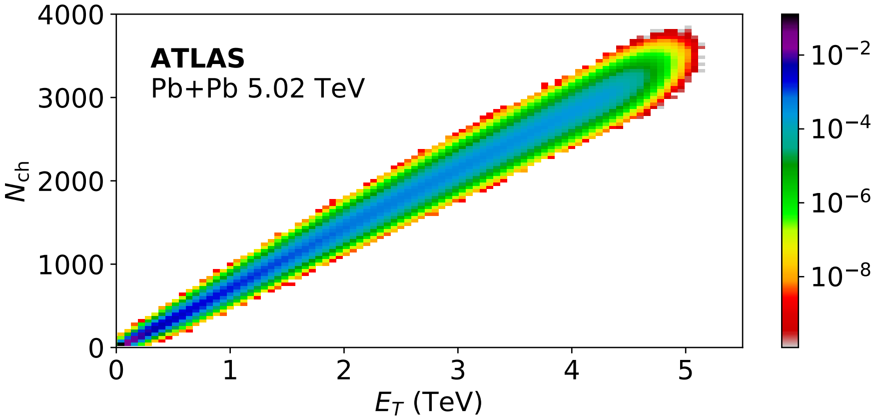

Figure 6.1: Normalized histogram of the distribution of (E_T, N_{ch}) measured by the ATLAS collaboration [13] in Pb+Pb collisions at $\sqrt{s_{\mathrm{NN}}} = 5.02\,\mathrm{TeV}$. E_T denotes the transverse energy in the pseudorapidity window $3.2 < |\eta| < 4.9$ and N_{ch} the number of reconstructed tracks of charged particles in the pseudorapidity window $|\eta| < 2.5$.

The key assumption of the method is that the distribution of $(N_1, ..., N_p)$ *at fixed impact parameter* is a multivariate Gaussian. This can be justified using the central limit theorem. As we argued in Chapter 4, the origin of multiplicity fluctuations lies in the early stage of collision dynamics. Consider the processes in this stage that induce particle production. If they occur at different points in the transverse plane, then, due to the ultrarelativistic regime, they are causally disconnected from each other. Hence, measured particle multiplicities can be considered a superposition of independent contributions. Moreover, the number of contributions is arguably large: there are more than 3000 particles that contribute to N_{ch} in Fig. 6.1, and an even larger number of particles that contribute to E_T. The centrality observables are thus made up by a superposition of a large number of independent contributions, which is the condition under which the central limit theorem applies. The validity of Gaussian fluctuations will be checked in Chapter 7.

When looking at a fixed impact parameter b, one can alternatively, and equivalently, fix the b-centrality c_b. As we saw in Chapter 3, impact parameter and b-centrality are related through the simple geometric relation given in Eq. (3.3). It is in fact often convenient to trade the impact parameter for the b-centrality: Since c_b is essentially the cumulative distribution of b, its probability distribution $P(c_b)$ is by construction uniform and equal to unity in the interval $[0, 1]$. Let us therefore reinstate in terms of c_b our key assumption of a multivariate Gaussian for the distribution of $(N_1, ..., N_p)$ at fixed impact parameter:

$$P(N_1, ..., N_p|c_b) = \frac{\exp\left(-\frac{1}{2}(N_i - \bar{N}_i(c_b))\Sigma^{-1}_{ij}(c_b)(N_j - \bar{N}_j(c_b))\right)}{\sqrt{(2\pi)^p|\mathbf{\Sigma}(c_b)|}}, \quad (6.1)$$

where, in the exponential, we use the Einstein sum convention over the repeated indices i and j. We denote by $\bar{N}_i$ the mean, or average, value of N_i and by $\mathbf{\Sigma} = (\Sigma_{ij})$ the covariance matrix:

$$\bar{N}_i = \langle N_i \rangle \quad (6.2)$$

$$\begin{aligned} \Sigma_{ij} &= \langle (N_i - \bar{N}_i)(N_j - \bar{N}_j) \rangle \\ &= \langle N_i N_j \rangle - \bar{N}_i \bar{N}_j. \end{aligned} \quad (6.3)$$

Here, angular brackets denote an average over events with the same impact parameter. In Eq. (6.1) we call by $\mathbf{\Sigma}^{-1}$ the inverse matrix of $\mathbf{\Sigma}$ and by $|\mathbf{\Sigma}|$ its determinant. The observed distribution $P(N_1, ..., N_p)$ is then obtained by integrating over c_b,

$$\begin{aligned} P(N_1, ..., N_p) &= \int_0^1 \mathrm{d}c_b\, P(N_1, ..., N_p|c_b) P(c_b) \\ &= \int_0^1 \mathrm{d}c_b\, P(N_1, ..., N_p|c_b), \end{aligned} \quad (6.4)$$

where we have explicitly used that the probability distribution of c_b is uniform.

We assume $\bar{N}_i$ and Σ_{ij} to be smooth functions of c_b and choose to parametrize them as exponentials of polynomials with degree $n_{\max}$ and $m_{\max}$, respectively:

$$\bar{N}_i(c_b) = \bar{N}_i(0) \exp\left(- \sum_{n=1}^{n_{\max}} a_{i;n} c_b^n \right) \tag{6.5}$$

$$\Sigma_{ij}(c_b) = \Sigma_{ij}(0) \exp\left(- \sum_{m=1}^{m_{\max}} A_{ij;m} c_b^m \right) \tag{6.6}$$

Here, $\bar{N}_i(0)$, $\Sigma_{ij}(0)$, $a_{i;n}$ and $A_{ij;m}$ are free parameters that are obtained by fitting Eq. (6.4) to data, e.g. to the ATLAS data in Fig. 6.1 in the case of $p = 2$. Two comments are in order. Firstly, the choice for this particular parametrization is rooted in our wish to constrain $\bar{N}_i$ and Σ_{ij} to positive functions. Any other parametrization that ensures positivity is just as adequate. The $\bar{N}_i$ are positive as they are centrality observables (number of particles or energy) while at least for $p = 2$, all elements of $\boldsymbol{\Sigma}$ are positive as well because there is a positive correlation between two distinct centrality observables, as can be seen in Fig. 6.1. Secondly, we do *not* impose explicitly in Eq. (6.5) that the N_i be monotonously decreasing as a function of centrality. As we will see in Chapter 8, this conveniently comes out automatically from the fit.

We will see in Chapter 7 that the mean values $\bar{N}_i$ can be reconstructed precisely for all impact parameters. On the other hand, one can reconstruct $\boldsymbol{\Sigma}$ accurately for $b = 0$ only. Let us now investigate in more detail which quantities can be reconstructed from the the distribution of $(N_1, ..., N_p)$ and which cannot.

Consider the tip of the distribution in Fig. 6.1, which corresponds to the highest values of N_i. This part of the distribution results from contributions with $c_b = 0$ only, which is why $\bar{N}_i(0)$ and $\Sigma_{ij}(0)$ can be reconstructed. Note also how the ellipse in Fig. 1.1 closely fits the tip of the distribution.

Any point in the bulk of the distribution, however, receives contributions from collisions at different c_b, which are superposed. This leads to a loss of information. In order to understand this qualitatively, consider for $p = 2$ the parametric curve $(\bar{N}_1(c_b), \bar{N}_2(c_b))$, which we call the ridge line, and which is illustrated as a solid line in Fig. 6.2. When cutting perpendicularly to it, the maximum value of probability is on the ridge line. Only displacements perpendicular to the ridge line are due to fluctuations of N_i at fixed impact parameter (which we are after), while displacements parallel to it might also result from a variation of the impact parameter. Therefore, we can only reconstruct the *projection of the covariance matrix orthogonal to the ridge line.* This idea will now be formalized in the general multivariable case.

Consider a point $(N_1, ..., N_p)$ close to the ridge line. To each component N_i, one can assign an experimental centrality c_i through

$$N_i = \bar{N}(c_i). \tag{6.7}$$

For $p = 2$, this is illustrated in Fig. 6.2. Since we are close to the ridge line, we can linearize around c_b:

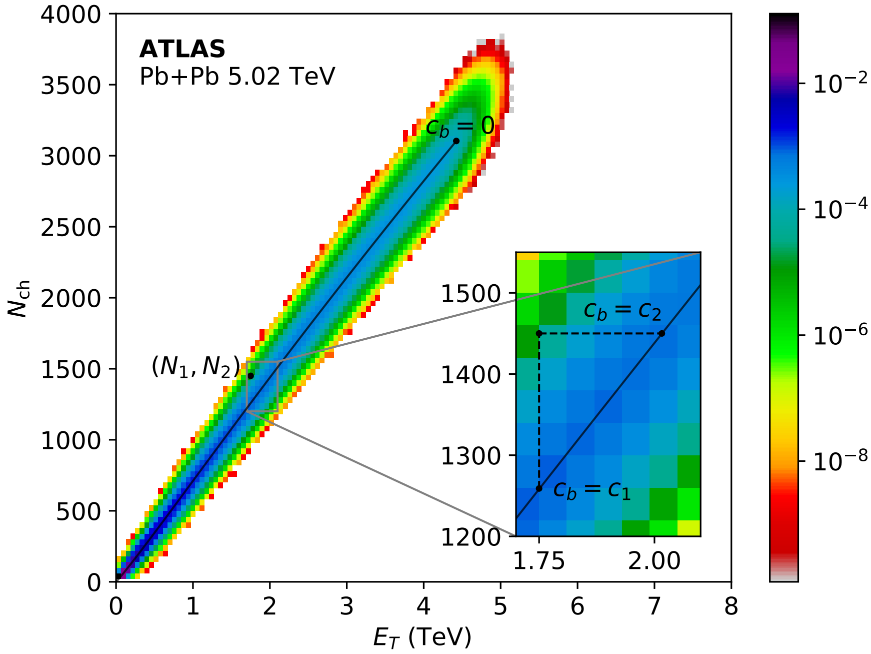

Figure 6.2: Illustration of the quantities in Eq. (6.7). The line is the parametric curve $(\bar{N}_1(c_b), \bar{N}_2(c_b))$, or ridge line (see text). For a given point (N_1, N_2) close to the ridge line, c_1 and c_2 defined by Eq. (6.7) are obtained by projections onto the ridge line.

$$N_i - \bar{N}_i(c_b) = \bar{N}(c_i) - \bar{N}(c_b) = (c_i - c_b)\bar{N}_i'(c_b), \tag{6.8}$$

where we denote by $\bar{N}_i'$ the derivative of $\bar{N}_i$ with respect to c_b, and substitute Eq. (6.8) in Eq. (6.1):

$$P(N_1, ..., N_p|c_b) \propto \exp\left(-\frac{1}{2}\sum_{ij}(c_i - c_b)\bar{N}_i'\Sigma_{ij}^{-1}\bar{N}_j'(c_j - c_b)\right), \tag{6.9}$$

where we omitted the dependence of $\bar{N}_i'$ and Σ_{ij}^{-1} on c_b. This has been done on purpose: The contribution of this integrand mainly comes from a narrow range of c_b close to the c_i, in which we expect $\bar{N}_i'$ and Σ_{ij}^{-1} to hardly vary with respect to the impact parameter. With this approximation, we obtain a Gaussian integral for the distribution of $(N_1, ..., N_p)$:

$$P(N_1, ..., N_p|c_b) \propto \exp\left(-\frac{1}{2}\sum_{ij} c_i \Pi_{ij} c_j\right), \tag{6.10}$$

where we neglected the pre-exponential factor and introduced

$$\Pi_{ij} \equiv \bar{N}'_i \Sigma^{-1}_{ij} \bar{N}'_j - \frac{\left(\sum_\alpha \bar{N}'_i \Sigma^{-1}_{i\alpha} \bar{N}'_\alpha\right)\left(\sum_\beta \bar{N}'_j \Sigma^{-1}_{j\beta} \bar{N}'_\beta\right)}{\sum\limits_{\alpha\beta} \bar{N}'_\alpha \Sigma^{-1}_{\alpha\beta} \bar{N}'_\beta} \tag{6.11}$$

$\mathbf{\Pi}$ constitutes the quantity that can be reconstructed for all impact parameters. Note that it is a symmetric $p \times p$ matrix and satisfies $\sum_i \Pi_{ij} = 0$ for all j, meaning that all rows and columns add up to zero. Using this property, one can rewrite Eq. (6.10) thusly:

$$P(N_1, ..., N_p) \propto \exp\left(-\frac{1}{2} \sum_{i>1, j>1} (c_i - c_1)\Pi_{ij}(c_j - c_1)\right) \tag{6.12}$$

In this form, one can readily see that the distribution of $(N_1, ..., N_p)$ is a function of the $p-1$ variables $c_i - c_1$. Physically, $\mathbf{\Pi}$ corresponds to the projection of $\mathbf{\Sigma}$ to the $(p-1)$-dimensional subspace orthogonal to the ridge line. For $p = 2$, one obtains

$$\mathbf{\Pi} = \frac{1}{\sigma_\perp^2} \begin{pmatrix} 1 & -1 \\ -1 & 1 \end{pmatrix} \tag{6.13}$$

where we introduced

$$\sigma_\perp(c_b) \equiv \sqrt{\frac{\Sigma_{11}(c_b)}{\bar{N}'_1(c_b)^2} + \frac{\Sigma_{22}(c_b)}{\bar{N}'_2(c_b)^2} - 2\frac{\Sigma_{12}(c_b)}{\bar{N}'_1(c_b)\bar{N}'_2(c_b)}}. \tag{6.14}$$

Here, c_b can denote any b-centrality between c_1 and c_2 (see Fig. 6.2), since we neglected the variation of the covariance matrix in this interval. Inserting Eq. (6.14) into Eq. (6.12), one obtains for $p = 2$:

$$P(N_1, N_2) \propto \exp\left(-\frac{\delta c^2}{2\sigma_\perp^2(c_b)}\right), \tag{6.15}$$

where we defined $\delta c = c_1 - c_2$. In the case of ATLAS data, δc denotes the difference between the centralities according to E_T and N_{ch}, while $\sigma_\perp$ quantifies the width of the distribution of (E_T, N_{ch}) in units of centrality. We shall see in Chapter 7 that $\sigma_\perp$ is accurately reconstructed for $c_b > 0$, and Σ_{ij} only for $c_b = 0$.

Before concluding this chapter, it is worth mentioning that, given the experimental distribution of (N_1, N_2), one can consider the projected distributions $P(N_1)$ and $P(N_2)$ and apply the single-variable method [26] to them. For a single observable N, its probability distribution at fixed b-centrality reads

$$P(N|c_b) = \frac{\exp\left(-\frac{1}{2\sigma^2(c_b)}(N - \bar{N}(c_b))^2\right)}{\sqrt{2\pi\sigma^2(c_b)}}, \tag{6.16}$$

where $\sigma^2(c_b) = \langle N^2 \rangle (c_b) - \bar{N}^2(c_b)$ denotes the variance of the observable at fixed impact parameter. This function, however, cannot be reconstructed for $c_b > 0$. Indeed, $\mathbf{\Pi} = 0$ for $p = 1$, cf. Eq. (6.11). Instead, one needs to make an assumption on the impact parameter dependence of σ^2, e.g. $\sigma^2(c_b) \propto \bar{N}(c_b)$ [26]. What makes the reconstruction from 2D data more powerful than considering 1D projections is the possibility to gain information on the full covariance structure of fluctuations at $b = 0$, i.e. the off-diagonal entry Σ_{12}, as well as on the projection $\sigma_\perp$ for $b > 0$.

7

VALIDATION

In this chapter, we will demonstrate the validity of the reconstruction described in Chapter 6 using fake data generated with the TRENTo 3D model of initial conditions (see Section 4.2 for details). This state-of-the-art model allows an event-by-event computation of the entropy density profile $s(x, y, \eta_s)$ at an early time after the collision. (x, y) denotes a point in the transverse plane and η_s the space-time rapidity, which is approximately equal to the pseudorapidity, cf. the discussion below Eq. (2.4). The entropy density is computed on a (x, y, η_s)-lattice whose size is adjustable. In the x- and y-direction, we go from $-9\,\mathrm{fm}$ to $9\,\mathrm{fm}$ in steps of $0.2\,\mathrm{fm}$, while η_s is discretized from -5 to 5 in steps of 0.2.

For each generated event, one can obtain estimators for E_T and N_{ch} as follows. In the high-temperature limit, one can describe the quark-gluon plasma as an ideal gas of massless particles. In this approximation, final-state charged-particle multiplicity is proportional to the initial entropy of the fireball [27]. In an attempt to mimic the pseudorapidity window of the ATLAS detector measuring N_{ch}, we choose

$$N_{\mathrm{ch}} = \mathcal{N}_n \int_{\eta_{\min}}^{\eta_{\max}} \mathrm{d}\eta_s \int_{\mathbb{R}^2} \mathrm{d}^2 x\, s(\vec{x}, \eta_s) \tag{7.1}$$

with $\eta_{\min} = -2.5$, $\eta_{\max} = 2.5$ as a proxy for the final-state charged-particle multiplicity measured by the detector. $\mathcal{N}_n$ denotes some proportionality constant.

As for the energy deposit into a specific solid angle region, we assume that the final-state energy density is proportional to the initial energy density. For a thermodynamic equation of state of the ideal gas form, in which pressure and temperature are related through $p \sim T^4$, the energy density scales with the power $4/3$ with the entropy density. This motivates the following estimator for the final-state transverse energy deposit:

$$E_T = \mathcal{N}_e \int_{\eta_{\min} < |\eta_s| < \eta_{\max}} \mathrm{d}\eta_s \int_{\mathbb{R}^2} \mathrm{d}^2 x\, s(\vec{x}, \eta_s)^{4/3} \tag{7.2}$$

The pseudorapidity range of the corresponding ATLAS detector is given by $\eta_{\min} = 3.2$, $\eta_{\max} = 4.9$. The proportionality constants $\mathcal{N}_n$ and $\mathcal{N}_e$ are used to normalize E_T and N_{ch} in such a way that their mean values for central collisions coincide with those reconstructed from ATLAS data (see Table 8.1).

We generate $1.2 \cdot 10^6$ minimum-bias Pb+Pb collisions at $\sqrt{s_{\mathrm{NN}}} = 5.02\,\mathrm{TeV}$ and obtain values of E_T and N_{ch} for each collision. The resulting histogram is presented in Fig. 7.1 and looks roughly similar to the experimental distribution from ATLAS displayed in Fig. 6.1. In the following, we apply the 2D method of Bayesian reconstruction to this histogram.

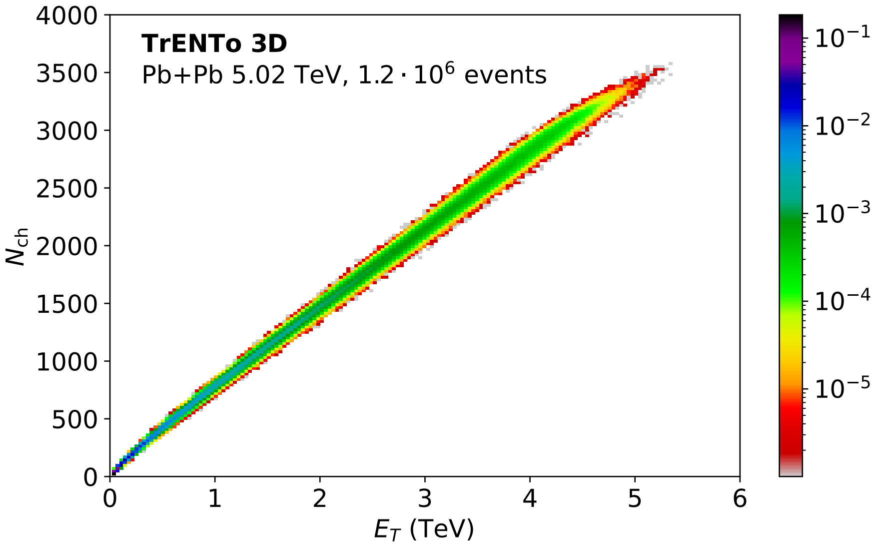

Figure 7.1: Normalized histogram of (E_T, N_{ch}) for $1.2 \cdot 10^6$ minimum-bias Pb+Pb collisions at $\sqrt{s_{\mathrm{NN}}} = 5.02\,\mathrm{TeV}$ generated using the TRENTo 3D model [20]. Note that the number of events is smaller by a factor ~ 140 than in the data shown in Fig. 1.1, and that we use a slightly finer binning in (E_T, N_{ch}).

In contrast to actual experimental data, we *do* know the impact parameter for each collision event obtained using TRENTo 3D, and we can further generate events at fixed impact parameter. This allows us to compare the reconstructed $\bar{N}_i(c_b)$ and $\Sigma_{ij}(c_b)$ to a direct calculation of these quantities obtained by averaging over events at fixed impact parameter.

As a first step, one should check for the TRENTo 3D model the assumption of Gaussian fluctuations that we make in Chapter 6 in order to derive our method of Bayesian reconstruction. We do this by running the model for several fixed impact parameters. The resulting distributions are displayed in the left panels of Fig. 7.2. On the right, we present the result of fitting a bivariate Gaussian to the data. The quality of the fits, quantified by a standard χ^2, decreases as the impact parameter increases. The Gaussian approximation captures the distributions on the left fairly well, except for the bottom panel, which corresponds to $b = 12\,\mathrm{fm}$. Not only does the Gaussian (by its nature) not achieve to reproduce the non-elliptical shape of the true distribution, but it extends to negative values of E_T and N_{ch} as well, which are unphysical. It should be pointed out that this issue has been successfully overcome for the single-variable case by replacing the Gaussian distribution in Eq. (6.1) with a Γ-distribution [28]. However, we did not find a straightforward way of generalizing this approach to the multivariable case.

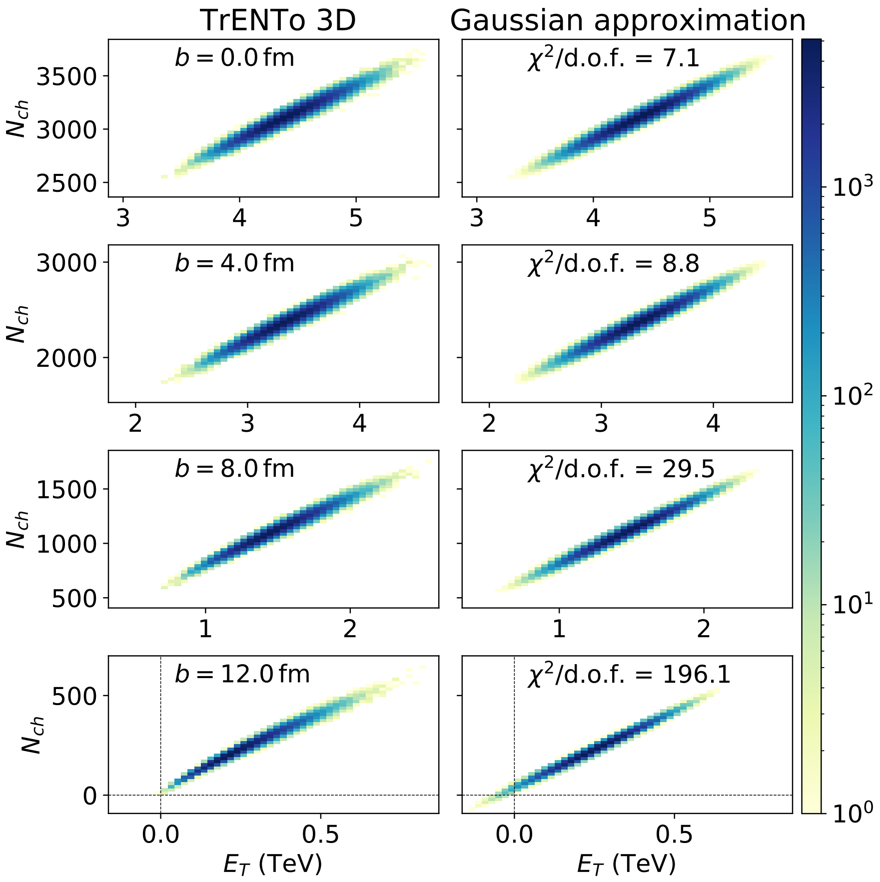

Figure 7.2: *Left:* Histogram of the distribution of (E_T, N_{ch}) from the TRENTo 3D model of initial conditions [20] (see Sec. 4.2 for details) in Pb+Pb collisions at $\sqrt{s_{\text{NN}}} = 5.02\,\text{TeV}$ for fixed values of the impact parameter, with 10^5 events each, from top to bottom: $b = 0, 4, 8, 12\,\text{fm}$. *Right:* two-dimensional Gaussian fits to these distributions. We indicate the χ^2 of each fit.

As the assumption of Gaussian fluctuations breaks down for peripheral collisions, we need to exclude them from the fit. The excluded events are represented by a grey square at the bottom left of Fig. 7.1; they correspond to events with $E_T < E_{T,\text{min}}$ and $N_{\text{ch}} < N_{\text{ch,min}}$, where $E_{T,\text{min}}$ and $N_{\text{ch,min}}$ denote cutoffs specified in Table 8.1. We chose the cutoffs in such a way that excluded events make up $\sim 40\,\%$ of all events.

Next, we fit according to the Bayesian reconstruction method introduced in Chapter 6 with $n_{\text{max}} = 3$ and $m_{\text{max}} = 2$ in Eq. (6.6). This leads to four parameters for each of $\bar{E}_T(c_b)$ and $\bar{N}_{\text{ch}}(c_b)$ as well as three parameters for each element of $\mathbf{\Sigma}(c_b)$, or 17 fit parameters in total. Furthermore, we need the total Pb+Pb inelastic cross section σ_{PbPb} in order to convert impact parameters to b-centrality according to Eq. (3.3). We evaluate σ_{PbPb} in TRENTo 3D by computing the fraction $f(b)$ of events with an impact parameter below b, with b small enough that the probability of collision (see Fig. 3.2) is close to unity. Then $\sigma_{\text{PbPb}} = \pi b^2/f(b)$. We obtain $\sigma_{\text{PbPb}} = 800(2)\,\text{fm}^2$.

In Fig. 7.3, we present the reconstructions for $N_{\text{ch}}(b)$, $E_T(b)$ and $\sigma_\perp(b)$, namely those functions for which we motivated in Chapter 6 that they can be reconstructed for all impact parameters. In the lower panels, we plot the ratio of reconstructed values of the values obtained through a direct calculation in order to assess the quality of the reconstruction. Note that since we have excluded peripheral events, one cannot trust the outcome of the reconstruction for b too large. We expect the reconstruction to be robust for values of b such that at least 90 % of events with this impact parameter are included in the fit. Those b for which this no longer holds are represented by a light grey band in Fig. 7.3. The dark grey band is defined by $\bar{E}_T(b) < E_{\text{T,min}}$. The obtained fit parameters are presented in Table 8.1 together with the result from ATLAS data.

Indeed, $N_{\text{ch}}(b)$ and $E_T(b)$ are accurately reconstructed to a precision of at most 1 %. Note that those two quantities can be reconstructed equally well by considering 1D projections of (E_T, N_{ch})-distribution and performing a 1D reconstruction, as outlined at the end of Chapter 6. As can be seen from Fig. 7.3, the 2D reconstruction is similarly precise as the 1D reconstruction.

The width of the (E_T, N_{ch})-distribution, measured by $\sigma_\perp(b)$, is robustly reconstructed for all impact parameters as well, within a precision of a few percent. On the other hand, the elements of $\mathbf{\Sigma}(b)$ cannot be accurately reconstructed except for $b = 0$, as is confirmed by Fig. 7.4, in which we plot the reconstructed and directly calculated $\Sigma_{ij}(b)$. For $b = 0$, $\Sigma_{ij}(0)$ is reconstructed with an error of about 5 %, while the quality of reconstruction decreases significantly for non-vanishing impact parameters. This can also be seen from the ellipses we plot on top of the histogram in Fig. 7.5 for several impact parameters. They correspond to the 99 % confidence ellipses for the corresponding impact parameter b, meaning that 99 % of the events with impact parameter b lie inside the ellipse defined by the set of (N_1, N_2) that satisfy

$$(N_i - \bar{N}_i(b))\Sigma_{ij}^{-1}(b)(N_j - \bar{N}_j(b)) = -2\ln(1-p), \quad p = 0.99. \quad (7.3)$$

Both the direct calculation and the Bayesian reconstruction give rise to a confidence ellipse. There is a good agreement between them for $b = 0$, but an increasing discrepancy can be observed for increasing impact parameters. Note, however, how the reconstructed ellipses, while differing significantly from the directly computed ones (ie. the *true* ones), still capture the width of the (E_T, N_{ch})-distribution correctly for all impact parameters. This demonstrates as well that there is a component of the covariance matrix that can be reconstructed for all b.

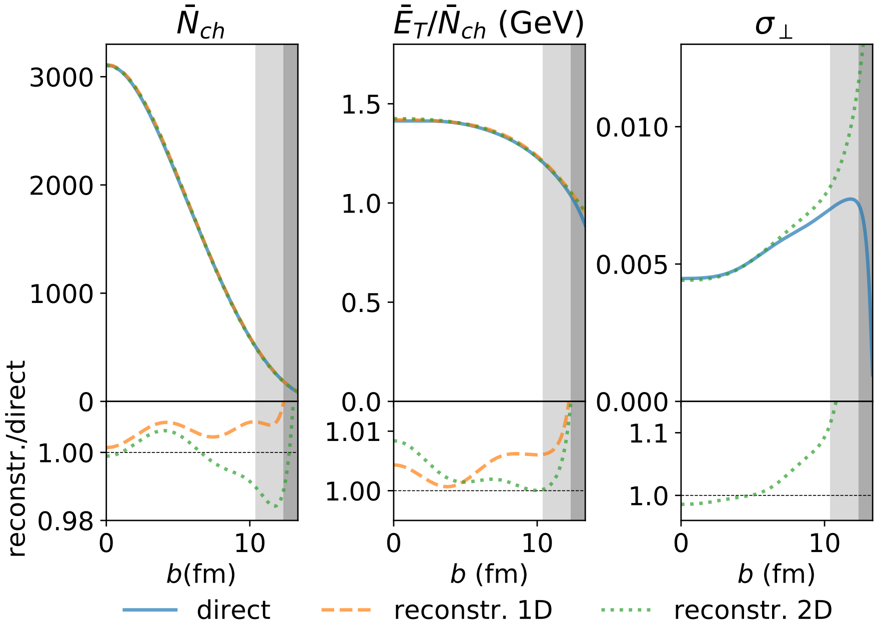

Figure 7.3: Left to right: $\bar{N}_{\text{ch}}(b)$, $\bar{E}_T(b)/\bar{N}_{\text{ch}}(b)$ and $\sigma_\perp(b)$ (defined by (Eq. (6.14)) versus impact parameter. The vertical grey bands indicate the limits above which the reconstruction can no longer be trusted because peripheral events have been excluded from the fit (see text for details). The full lines correspond to the direct calculation, where one averages over events at fixed b. The derivatives $\bar{N}'_{\text{ch}}(c_b)$ and $\bar{E}'_T(c_b)$ in (Eq. (6.14)) are evaluated by fitting $\bar{N}_{\text{ch}}(c_b)$ and $\bar{E}_T(c_b)$ with a smooth curve and taking the derivative of the fit. The dashed lines in the left and middle panels correspond to the values reconstructed using the projected distributions of E_T and N_{ch}, following the same method as in [26]. The dotted lines correspond to the values reconstructed using the distribution $P(E_T, N_{\text{ch}})$, which is done as explained in Chapter 6. The bottom panels display the ratio between the reconstructed value and the direct calculation.

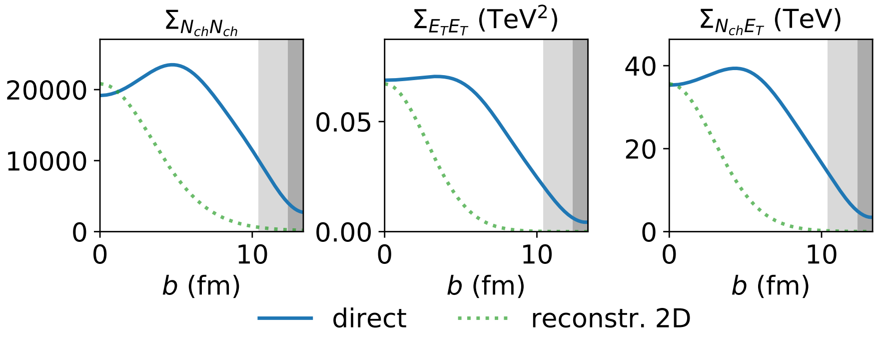

Figure 7.4: Elements of the covariance matrix as a function of impact parameter in the TRENTo 3D model. Left to right: Variance of N_{ch}, variance of E_T, covariance of N_{ch} and E_T. The full lines correspond to the direct calculation, where one averages over events at fixed b. The dotted lines correspond to the reconstructed values.

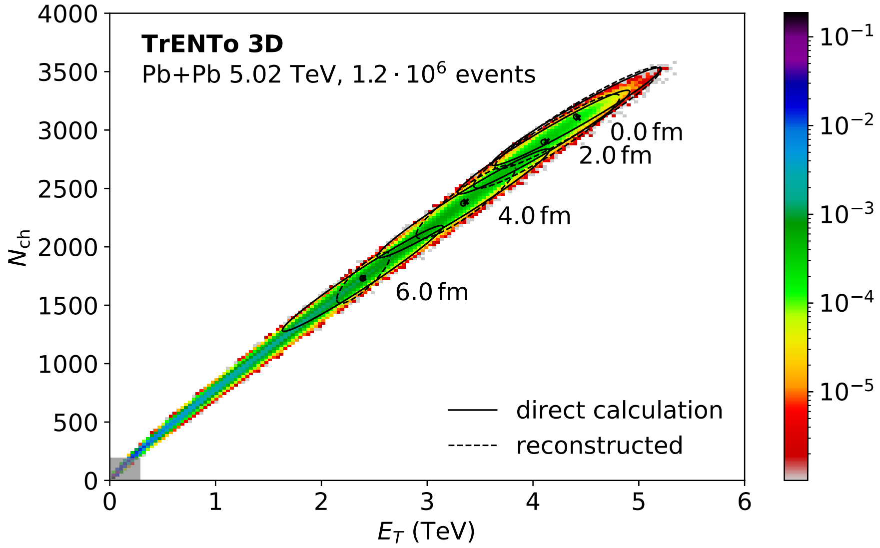

Figure 7.5: Normalized histogram of (E_T, N_{ch}) for $1.2 \cdot 10^6$ minimum-bias Pb+Pb collisions at $\sqrt{s_{\mathrm{NN}}} = 5.02\,\mathrm{TeV}$ generated using the TRENTo 3D model [20]. The grey square at the bottom left represents the part of the histogram that is excluded from the fit, corresponding to the most peripheral collisions. The ellipses correspond to the 99 % confidence ellipses for fixed values of $b = 0, 2, 4, 6$ fm, calculated directly (full lines) or from the Bayesian reconstruction (dashed lines). The points corresponding to the average value of (E_T, N_{ch}) are represented as circles (direct calculation) and as crosses (reconstruction).

8

APPLICATION TO ATLAS DATA

Now that we have validated our Bayesian reconstruction method using the TRENTo 3D model of initial conditions, we apply it to the ATLAS data in Fig. 6.1. We use the same cuts as for TRENTo 3D in Chapter 7 to exclude peripheral collisions.

The best fit parameters are presented in Table 8.1. It contains

- the impact parameter dependence of the mean transverse energy $\bar{E}_T$ and of the mean charged-particle multiplicity $\bar{N}_{\text{ch}}$,
- the variances of E_T and N_{ch} as well as the covariance of E_T and N_{ch} for central collisions, i.e. $b = 0$,
- the impact parameter dependence of the width $\sigma_\perp$ defined by Eq. (6.14).

We expect the uncertainty on our result to be dominated by non-gaussian fluctuations, which are not captured by Eq. (6.1). While we explicitly exclude peripheral events to keep non-gaussian contributions in check, we expect that this effect sets in gradually with increasing impact parameter and hence cannot be completely removed with a sharp cutoff. Therefore, in order to estimate the error on our result, we first check the robustness of the reconstruction by varying the cutoffs in E_T and N_{ch} such that the fraction of excluded events varies from 35 % to 45 % of all events. We find that the result variations are significantly smaller than the difference between the direct calculation and the reconstruction in TRENTo 3D. For this reason, we estimate the relative uncertainty on our results as the maximum relative error between the directly calculated and the reconstructed value in TRENTo 3D.

Before discussing in detail the results, we turn to Fig. 8.1, which displays the quality of the fit, measured by the ratio between the fit and ATLAS data. We obtain an excellent fit around the ridge line with agreement between fit and data to percent level. Only far away from the ridge at the tip of the distribution is the quality compromised. These parts, however, make up less than 1 % of all events.

In the remainder of this chapter, we discuss our results for the mean values of N_{ch} and E_T, which are results that could have been obtained as well from the 1D reconstruction. Results involving $\mathbf{\Sigma}$, which constitute our most important results, will be discussed in Chapter 9.

In Fig. 8.2 we plot the centrality dependence of $\bar{N}_{\text{ch}}$. Note that in order to convert b-centrality to impact parameters, we need the

Table 8.1: Values of fit parameters, as defined by Eq. (6.6), for ATLAS data shown in Fig. 6.1, and for the TRENTo 3D calculation shown in Fig. 7.1. This model calculation has been calibrated in such a way that the first two entries are the same as in experiment. The cutoffs used are $E_{T,\mathrm{min}} = 0.289\,\mathrm{TeV}$, $N_{\mathrm{ch,min}} = 194.39$. The uncertainties for the first five parameters are estimated using the relative difference between the direct calculation and its reconstruction, see text for details. As far as the coefficients of the polynomials in Eq. (6.6), we omitted error bars because the individual uncertainties are not reflective of the uncertainty of the corresponding physical observable, e.g. $\bar{E}_T$, for a given impact parameter.

	ATLAS	TRENTo 3D
$\bar{E}_T(0)$ (TeV)	$4.424(34)$	$4.424(34)$
$\bar{N}_{\mathrm{ch}}(0)$	$3.104(6) \cdot 10^3$	$3.104(6) \cdot 10^3$
$\Sigma_{E_T E_T}(0)$ (TeV^2)	$2.24(15) \cdot 10^{-2}$	$6.72(44) \cdot 10^{-2}$
$\Sigma_{N_{\mathrm{ch}} N_{\mathrm{ch}}}(0)$	$1.926(79) \cdot 10^4$	$2.083(85) \cdot 10^4$
$\Sigma_{E_T N_{\mathrm{ch}}}(0)$ (TeV)	$1.47(11) \cdot 10^1$	$3.57(25) \cdot 10^1$
$a_{E_T,1}$	4.00	4.41
$a_{N_{\mathrm{ch}},1}$	3.77	4.27
$a_{E_T,2}$	−1.49	−1.06
$a_{N_{\mathrm{ch}},2}$	−0.91	−1.64
$a_{E_T,3}$	3.97	4.09
$a_{N_{\mathrm{ch}},3}$	3.86	4.04
$A_{E_T,E_T,1}$	4.08	16.60
$A_{N_{\mathrm{ch}},N_{\mathrm{ch}},1}$	7.18	10.58
$A_{E_T,N_{\mathrm{ch}},1}$	7.48	14.60
$A_{E_T,E_T,2}$	1.18	−3.37
$A_{N_{\mathrm{ch}},N_{\mathrm{ch}},2}$	−1.89	−5.38
$A_{E_T,N_{\mathrm{ch}},2}$	1.32	−5.44

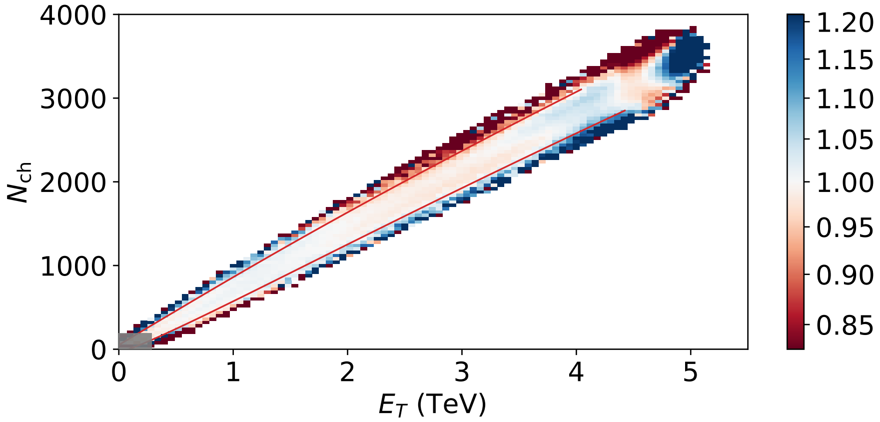

Figure 8.1: Ratio of the fit to ATLAS data in Fig. 6.1. As in Fig. 7.1, the grey square at the bottom left represents the part of the histogram that is excluded from the fit, corresponding to the most peripheral collisions. The lines correspond to contours with $\delta c = 2.6\,\sigma_\perp$ in (6.15), so that the region between the lines contains $\sim 99\%$ of the events. Specifically, the upper and lower lines are the parametric curves $(\bar{E}_T(c_b) + 2.6\sigma_\perp(c_b)\bar{E}'_T(c_b), \bar{N}_{\rm ch}(c_b))$, and $(\bar{E}_T(c_b), \bar{N}_{\rm ch}(c_b) + 2.6\sigma_\perp(c_b)\bar{N}'_{\rm ch}(c_b))$.

inelastic Pb+Pb cross section $\sigma_{\rm PbPb} = 767\,{\rm fm}^2$ extracted from a Glauber calculation [29] according to Eq. (4.3). For comparison, we also show the result from TRENTo 3D. The model reproduces ATLAS data well, albeit not perfectly, especially for mid-central to peripheral collisions.

In Fig. 8.3 we show the ratio $\bar{E}_T/\bar{N}_{\rm ch}$ as a function of the impact parameter, for ATLAS data as well as for TRENTo 3D. As it turns out, ATLAS data show a non-monotonic behaviour that is not reproduced by TRENTo 3D. This variation with b can be understood by decomposing the ratio as

$$\frac{\bar{E}_T(b)}{\bar{N}_{\rm ch}(b)} = \frac{\bar{E}_T(b)}{\bar{N}_{\rm FCAL}(b)} \frac{\bar{N}_{\rm FCAL}(b)}{\bar{N}_{\rm ch}(b)}, \tag{8.1}$$

where $\bar{N}_{\rm FCAL}$ denotes the mean hadron multiplicity of neutral and charged particles falling into the calorimeter acceptance. Before going on, note that $\bar{N}_{\rm FCAL}$ can be evaluated by integrating the pseudorapidity spectra of charged particles [30] over the acceptance covered by the calorimeter and multiplying by a factor $3/2$ to take into account neutral particles. Its average value at $b = 0$ is then evaluated by extrapolating linearly the values in the centrality intervals 0-5 % and 5-10 %, i.e. $\bar{N}_{\rm FCAL}(0) \approx (3/2)\bar{N}_{\rm FCAL}(0-5\,\%) - (1/2)\bar{N}_{\rm FCAL}(5-10\,\%)$. We obtain $\bar{N}_{\rm FCAL}(b=0) \approx 7930$.

Let us return to Eq. (8.1). The first factor, the ratio $\bar{E}_T/\bar{N}_{\rm FCAL}$ is equal to the energy deposit per hadron, which can be expected to be roughly equal to the transverse mass $m_t = \sqrt{p_t^2 + m^2}$. Indeed, using the fit parameters in Table 8.1, we obtain $\bar{E}_T(0)/\bar{N}_{\rm FCAL}(0) = 0.558\,{\rm GeV}$,

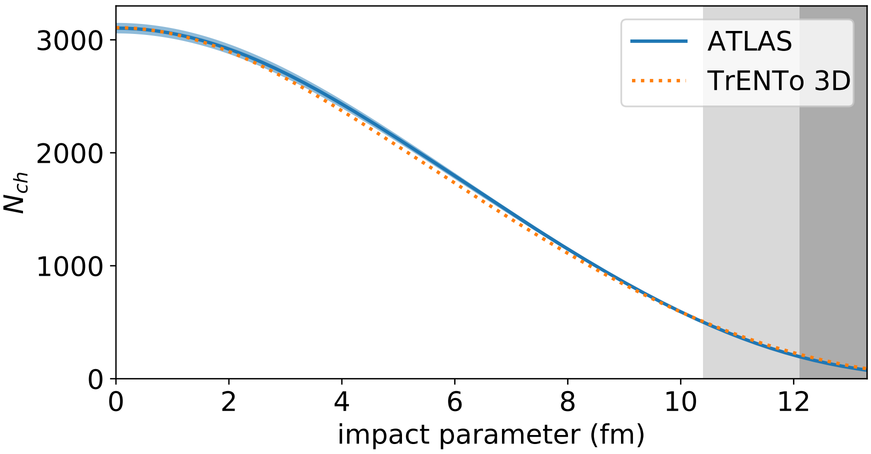

Figure 8.2: Variation of the mean charged multiplicity as a function of impact parameter. The full line is the value reconstructed using ATLAS data. The shaded band is our estimate of the error band (see text). The dashed line is the result of the direct TRENTo 3D calculation, shown as a full line in Fig. 7.3.

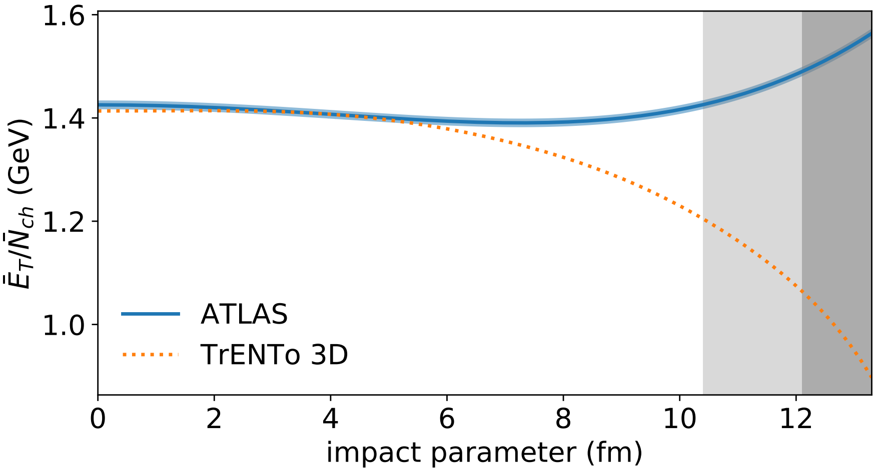

Figure 8.3: Same as Fig. 8.2 for the ratio of the mean transverse energy to the mean charged multiplicity.

which is the correct order of magnitude for the average transverse mass. In order to understand the non-monotonic behaviour exhibited in Fig. 8.3, it is important to note that the first factor in Eq. (8.1), essentially depends on the average transverse momentum $\langle p_t \rangle$, which decreases mildly as a function of b [31]. This is why the ATLAS curve decreases at first.

The second factor in Eq. (8.1), $\bar{N}_{\mathrm{FCAL}}/\bar{N}_{\mathrm{ch}}$ is (up to a factor $3/2$) the ratio between the multiplicity between the forward rapidity region (covered by the calorimeter) and the central rapidity region (covered by the N_{ch}-detector). Now, as b increases, the rapidity distribution becomes slightly broader [30]. Physically, this means that the stopping power between nuclei at finite b is not as strong as in central collisions. Therefore $\bar{N}_{\mathrm{FCAL}}/\bar{N}_{\mathrm{ch}}$ increases with b, overriding the decrease of $\langle p_t \rangle$ and yielding the increase seen for the ATLAS data. This second effect does not seem to be accurately reproduced by TRENTo 3D.

9

FLUCTUATIONS AT LARGE AND CENTRAL RAPIDITIES

In this chapter we turn to results involving the covariance matrix of E_T and N_{ch}. Given the pseudorapidity sectors covered by the detectors of these two centrality observables, we account for fluctuations in the central rapidity region probed by N_{ch}, in the large rapidity region probed by E_T as well as for their mutual correlation, which are the most important findings of this work.

Following the general discussion of fluctuations in Chapter 5, we first isolate the dynamical fluctuations of E_T and N_{ch} by subtracting out Poisson fluctuations in Section 9.1. We then present our results for central collisions in Section 9.2 and finally present the results for the impact parameter dependence in Section 9.3.

9.1 SUBTRACTION OF POISSON FLUCTUATIONS

As outlined in Chapter 5, when measuring centrality observables with detectors, there are Poisson contributions to the variances of the observables that are due to the fluctuating number of hadrons only. Therefore, we want to subtract them from the ATLAS measurement in order to isolate dynamical fluctuations.

For N_{ch}, the subtraction according to Eq. (5.2) is straightforward since all $x_i = 1$:

$$\Sigma_{N_{\text{ch}}N_{\text{ch}}}(b) \to \Sigma_{N_{\text{ch}}N_{\text{ch}}}(b) - \bar{N}_{\text{ch}}(b) \tag{9.1}$$

Hadronic decays, however, yield an uncertainty on this subtraction. If, for instance, a hadron decays into two particles that both fall into the detector acceptance, then the contribution of that hadron is $x_i = 2$ and not $x_i = 1$. The magnitude of this effect cannot be evaluated accurately since it depends on the hadronization mechanism. In the case of a fluid-dynamical model, for instance, it depends on the freeze-out temperature [32]. We expect this effect nevertheless to be modest and include the corresponding uncertainty in our error bar by assuming that there is a coefficient in front of $\bar{N}_{\text{ch}}$ in Eq. (9.1) that can vary between 1 and 1.2.

For the transverse energy, the expression in Eq. (5.2) with $\bar{N}_{\text{FCAL}}$ as the multiplicity and $x_i \simeq m_t = \sqrt{p_t^2 + m^2}$ for Poisson fluctuations reads $\langle m_t^2 \rangle \bar{N}_{\text{FCAL}}(b)$, where angular brackets denote an average over hadrons falling into the calorimeter acceptance. Using that $\bar{E}_T(b) =$

$\langle m_t \rangle \bar{N}_{\rm FCAL}(b)$ (see Eq. (5.7)), the expression for Poisson fluctuations can be decomposed as

$$\begin{aligned} \langle m_t^2 \rangle \bar{N}_{\rm FCAL}(b) &= \frac{\langle m_t^2 \rangle}{\langle m_t \rangle^2} \frac{\langle m_t \rangle^2 \bar{N}^2_{\rm FCAL}(b)}{\bar{N}_{\rm FCAL}(b)} \\ &= \frac{\langle m_t^2 \rangle}{\langle m_t \rangle^2} \frac{\bar{N}_{\rm ch}(b)}{\bar{N}_{\rm FCAL}(b)} \frac{\bar{E}^2_T(b)}{\bar{N}_{\rm ch}(b)}. \end{aligned} \tag{9.2}$$

We can evaluate the first term on the right-hand side of Eq. (9.2) using ALICE data on identified particle spectra [33], which yields $\langle m_t^2 \rangle / \langle m_t \rangle^2 \simeq 1.52$ for central collisions at $\sqrt{s_{\rm NN}} = 2.76\,\text{TeV}$. We neglect the dependence of this ratio on rapidity and on $\sqrt{s_{\rm NN}}$. The second term, $\bar{N}_{\rm ch}(b)/\bar{N}_{\rm FCAL}(b)$, is evaluated for central collisions using the value of $\bar{N}_{\rm ch}(0)$ in Table 8.1 and the estimate for $\bar{N}_{\rm FCAL}(0)$ obtained in Chapter 8. We neglect the dependence of this term on rapidity as well as on impact parameter. In total, these considerations yield the following expression for E_T for the subtraction of Poisson fluctuations:

$$\Sigma_{E_T E_T}(b) \to \Sigma_{E_T E_T}(b) - \alpha \frac{\bar{E}_T(b)^2}{\bar{N}_{\rm ch}(b)}, \tag{9.3}$$

where $\alpha \simeq 0.59$. We assign an uncertainty of $\pm 20\,\%$ to this factor α. Finally, since E_T and $N_{\rm ch}$ are measured in separate rapidity regions, no hadron contributes to E_T and $N_{\rm ch}$ simultaneously and hence Poisson fluctuations do not contribute to the covariance $\Sigma_{E_T, N_{\rm ch}}$.

Using the values in Table 8.1, the subtracted quantities in Eqs. (9.1) and (9.3) are 16 % and 17 % of the total. The fact that these two values are so similar is probably a coincidence.

9.2 FLUCTUATIONS OF $N_{\rm CH}$ AND E_T IN CENTRAL COLLISIONS

We now discuss fluctuations of $N_1 = E_T$ and $N_2 = N_{\rm ch}$ and their mutual correlation for central collisions. For this purpose, consider the relative covariance matrix $\boldsymbol{\sigma}$ [34], defined by

$$\sigma_{ij} \equiv \frac{\langle N_i N_j \rangle}{\langle N_i \rangle \langle N_j \rangle} - 1 = \frac{\Sigma_{ij}}{\bar{N}_i \bar{N}_j} \tag{9.4}$$

We refer to the diagonal elements of $\boldsymbol{\sigma}$ as *relative* variances.

The values of $\boldsymbol{\sigma}$ for ATLAS data are presented in Table 9.1. For each element σ_{ij}, we provide the value before and after the subtraction of Poisson fluctuations, as well as the result for TRENTo 3D for the sake of comparison.

One can infer from Table 9.1 that the relative fluctuations of E_T are smaller than those of $N_{\rm ch}$, both before and after the subtraction of Poisson fluctuations. This is the reason why E_T constitutes a better estimator of centrality than $N_{\rm ch}$ [13]. This is a non-trivial result that is not reproduced by TRENTo 3D. This model does reproduce the

Table 9.1: Relative covariance matrix $\boldsymbol{\sigma}$ of E_T and N_{ch}, defined by Eq. (9.4), for central Pb+Pb collisions ($b = 0$). For each element, the first line is the total covariance returned by the fit to data. The second line is the dynamical covariance obtained after subtracting Poisson fluctuations (see Section 9.1). The third line is the value in the (direct) TRENTo 3D calculation. The TRENTo 3D calculation returns a continuous density profile, and does not include hadronization. Therefore, the fluctuations calculated in this model are dynamical, and the subtraction of trivial fluctuations explained in Section 9.1 does not apply.

	$\sigma_{11} = \sigma_{E_T E_T}$	$\sigma_{22} = \sigma_{N_{\mathrm{ch}} N_{\mathrm{ch}}}$	$\sigma_{12} = \sigma_{E_T N_{\mathrm{ch}}}$
total	$1.14(8) \cdot 10^{-3}$	$2.00(9) \cdot 10^{-3}$	$1.07(8) \cdot 10^{-3}$
Poisson-subtracted	$0.96(6) \cdot 10^{-3}$	$1.68(2) \cdot 10^{-3}$	$1.07(8) \cdot 10^{-3}$
TRENTo 3D	$3.56 \cdot 10^{-3}$	$1.98 \cdot 10^{-3}$	$2.58 \cdot 10^{-3}$

variance of N_{ch} to a good approximation. This is not surprising since TRENTo 3D has been fitted to the distribution of charged multiplicity near mid-rapidity. On the other hand, it overestimates the variance of E_T by at least a factor 3.

There is no straightforward relation between the relative fluctuation of E_T and the corresponding multiplicity M (cf. Eq. (5.1)) in the same rapidity window. In the hydrodynamic framework, however, one expects them to be of the same order of magnitude because the multiplicity is proportional to the inital entropy density, which in turn is linked to energy density by virtue of the equation of state. In Chapter 10 we suggest an analysis to check the assumption of E_T-fluctuations being of the same order of magnitude as corresponding multiplicity fluctuations in the same rapidity window. If it turns out to be correct, our results imply that multiplicity fluctuations are smaller at large rapidity that around central rapidity.

It is useful to compare the results of Table 9.1 to values previously extracted from ATLAS data at $\sqrt{s_{\mathrm{NN}}} = 2.76\,\mathrm{TeV}$ using a 1D Bayesian reconstruction [26]. We subtract Poisson fluctuations using multiplicity densities measured by ALICE [30] and obtain $\sigma_{11} = 0.76 \cdot 10^{-3}$. This value is smaller than the one we obtained at 5.02 TeV (Table 9.1). Since the rapidity of the incoming nuclei increases by ~ 0.6 when passing from 2.76 TeV to 5.02 TeV, our result suggests that multiplicity fluctuations increase as a function of the rapidity difference with respect to the incoming nuclei.

The second important outcome of Table 9.1 is that E_T and N_{ch} are strongly correlated, even at the fixed impact parameter $b = 0$. This is illustrated by the elongated ellipse in Fig. 9.1. The correlation is significantly stronger after Poisson fluctuations have been subtracted out.

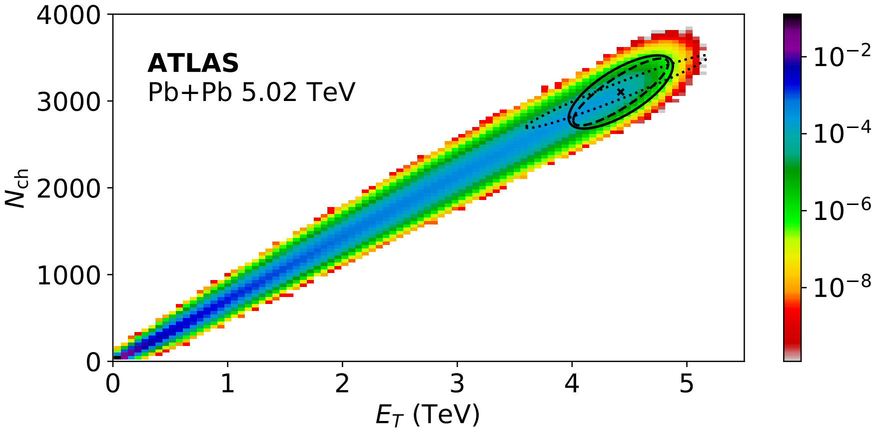

Figure 9.1: Full line: 99% confidence ellipse of zero impact parameter collisions, already shown in Fig. 1.1. The ellipse is defined by Eq. (7.3). The dashed line represents the ellipse, after subtraction of the contribution of Poisson fluctuations. The dotted line is the value from the TRENTo 3D calculation.

We now interpret the results of Table 9.1 using the simple statistical model of particle production presented in Chapter 5, which assumes nucleus-nucleus collisions at impact parameter b to produce N_s independent sources that in turn contribute to both E_T and N_{ch}. Building on Eq. (5.8), one easily finds for the relative covariance matrix (cf. Eq. (9.4)) under these assumptions:

$$\sigma_{ij} = \frac{\langle N_s^2 \rangle - \langle N_s \rangle^2}{\langle N_s \rangle^2} + \frac{1}{\langle N_s \rangle} \frac{\langle n_i n_j \rangle - \langle n_i \rangle \langle n_j \rangle}{\langle n_i \rangle \langle n_j \rangle}, \tag{9.5}$$

where we denote the contribution of a single source to E_T as n_1 and that to N_{ch} as n_2. We cannot uniquely determine all quantities on the right-hand side of Eq. (9.5) using Table 9.1 because there are more unknowns than equations. It is nonetheless possible to obtain non-trivial information from it.

Firstly, we have seen that $\sigma_{11} < \sigma_{22}$. Note that those two relative variances get the same contribution from fluctuations of the number N_s of sources, i.e. the first term in Eq. (9.5). This implies that the difference between the relative variances of E_T and N_{ch} is larger at the level of a single source.

Secondly, it is also possible to obtain non-trivial information on the correlation between n_1 and n_2, i.e. the contributions of a single source to E_T and N_{ch}. For instance, one can directly infer from Eq. (9.5) that they must be correlated, $\langle n_1 n_2 \rangle - \langle n_1 \rangle \langle n_2 \rangle > 0$, otherwise one would have $\sigma_{11} > \sigma_{12}$, which is at variance with the values in Table 9.1 after Poisson fluctuations have been subtracted out. One can even obtain a lower bound on the Pearson correlation coefficient r between n_1 and n_2, defined by $\langle n_1 n_2 \rangle - \langle n_1 \rangle \langle n_2 \rangle = r\sigma(n_1)\sigma(n_2)$, where $\sigma(n_i) \equiv$

$\sqrt{\langle n_i^2\rangle - \langle n_i\rangle^2}$ denotes the standard deviation of n_i. The lower bound is given by

$$r_{\min} = 2\frac{\sqrt{(\sigma_{12}-\sigma_{11})(\sigma_{22}-\sigma_{12})}}{\sigma_{22}-\sigma_{11}}, \tag{9.6}$$

which can be verified by checking that $r^2 - r^2_{\min}$ can be written as a square and is hence non-negative. Using the values in Table 9.1 and taking into account error bars from the reconstruction and from the uncertainty in the subtraction of Poisson fluctuations (cf. Section 9.1), we obtain $r_{\min} = 0.72(15)$.

Two effects may contribute to this strong correlation. Some sources may be stronger than others, e.g. those in the center of the interaction region, which is an effect not captured by the simple model discussed here. A stronger source leads to larger values of both n_1 and n_2, which is similar to fluctuations induced by the variation of the impact parameter. Alternatively, particle production from a single source is strongly correlated across rapidities. This is the interesting dynamical effect that one would like to isolate. More detailed modeling is necessary to disentangle the relative contributions of these two effects.

9.3 IMPACT PARAMETER DEPENDENCE OF FLUCTUATIONS

We have seen in Chapter 6 that the impact parameter dependence of the full covariance matrix $\mathbf{\Sigma}$ cannot be reconstructed, only the projection $\sigma_\perp$ perpendicular to the ridge line, defined in Eq. (6.14).

Figure 9.2 shows the b-dependence of $\sigma_\perp$, before and after the subtraction of Poisson fluctuations (cf. Section 9.1), as well as that for TRENTo 3D. The TRENTo 3D model underpredicts $\sigma_\perp$ for all values of impact parameter. This shows that the width of the distribution, as measured by $\sigma_\perp$, contains non-trivial dynamical information, which can be used to discriminate between models.

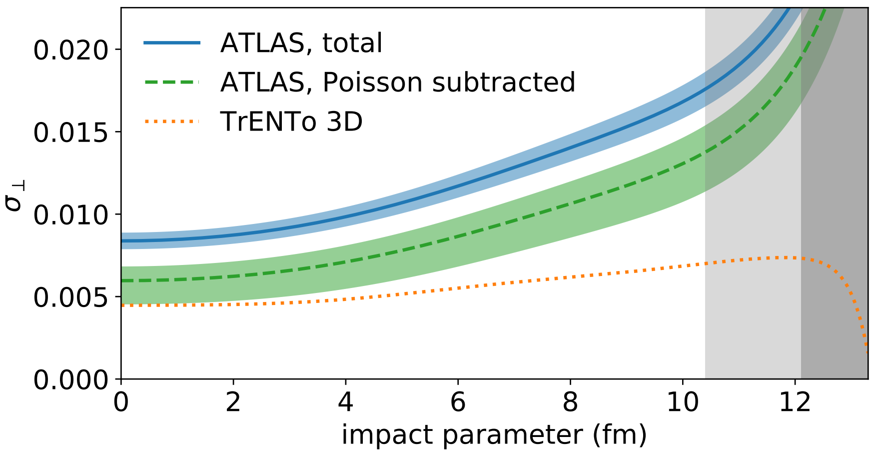

Figure 9.2: Same as Fig. 8.2 for the width of the distribution, defined by Eq. (6.14). Full line: before subtracting Poisson fluctuations. Dashed line: after subtracting Poisson fluctuations according to Eqs. (9.1) and (9.3). The shaded area is our estimate of the error on the reconstruction. Dotted line: value calculated in the TRENTo 3D model.

10

CONCLUSIONS AND PERSPECTIVES

In this work, we generalized a simple Bayesian method to the multivariable case in order to reconstruct fluctuations of centrality observables in nucleus-nucleus collisions as well as their mutual correlation. We did not need to rely on any specific model of collision dynamics, we only assumed Gaussian fluctuations for collisions at a fixed impact parameter, which are ensured by the central limit theorem for all but peripheral collisions. Given the distribution of p centrality observables $(N_1, ..., N_p)$ measured in different parts of the detector, we have shown that one can reconstruct the full covariance matrix of $(N_1, ..., N_p)$ for central collisions $(b = 0)$ as well as the impact parameter dependence of a $(p-1) \times (p-1)$ projection of the matrix. We validated the method for $p = 2$ using the state-of-the-art TRENTo 3D model of initial conditions. We applied the method to ATLAS data on the joint distribution of transverse energy and charged-particle multiplicity. Given that these two centrality observables cover different rapidity regions, the data set has allowed us to study correlations between large and central pseudorapidities. We have shown that dynamical fluctuations are smaller at large rapidities than around central rapidities. Moreover, we have found that particle production is strongly correlated across rapidity, even at fixed impact parameter. In addition, we have shown that the width of the distribution and its impact parameter dependence are not reproduced by our model calculation, so that this information can be used to rule out three-dimensional models of initial conditions.

Note that our method for studying rapidity-rapidity correlations is not restricted to multiplicities of charged-particle tracks, which are the traditional observables used to study rapidity correlations [8, 9]. But charged-particle tracks are typically only reconstructed around central rapidity, which limits the rapidity coverage of such studies. Our method, however, can be used as well with the transverse energy in a calorimeter, the multiplicity of pixel clusters [35] or the number of hits in a scintillator [4]. As long as the detector is large enough that dynamical fluctuations dominate over Poisson fluctuations, those observables provide quantitative information on fluctuations.

In order to interpret calorimeter measurements, one should first study how energy fluctuations relate to multiplicity fluctuations in the same rapidity window. As a first step, this can be done in the TRENTo 3D model by generating events at fixed impact parameter and evaluating $N_{\rm ch}$ and E_T according to Eqs. (7.1) and (7.2), but for the same pseudorapidity window. More importantly, the relationship between energy fluctuations and multiplicity fluctuations can also be studied experimentally by using the sum of transverse momenta of charged particles, $P_T \equiv \sum_{N_{\text{ch}}} p_t$, as a proxy for the transverse energy. This observable could be measured with N_{ch}-detectors since these measure momenta as well.

We conclude by suggesting explicit examples of similar analyses that could be done in the near future. Firstly, the transverse energy is usually defined as $E_T = E_F + E_B$, where E_F and E_B are the transverse energies of hadrons measured in forward and backward calorimeters [9, 35]. Given the distribution of (E_F, E_B), one could apply our method to the study of forward-backward rapidity correlations. In practice, applying our method to these data would be even simpler than the analysis in this work since forward and backward calorimeters are symmetric around midrapidity, and this symmetry reduces the number of fit parameters in the Bayesian analysis. Similarly, the ALICE collaboration could measure the distribution (V_{0A}, V_{0B}), where V_{0A} and V_{0C} are the multiplicities in backward and forward scintillators [4].

In this work, we applied our Bayesian method to $p = 2$ centrality observables only. More detailed information on the long-range rapidity structure of correlations could be obtained by extending the analysis to three variables. For instance, in the case of ATLAS data studied in this work, one could split the calorimeter into its forward and backward components to measure the joint distribution $(E_F, E_B, N_{\text{ch}})$. Similar analyses could be done with the CMS and ALICE detectors. Finally, our method could be applied to heavy-ion collisions at lower energies, to which the single-variable case of our method has recently been successfully applied [36, 37].

BIBLIOGRAPHY

[1] K. Adcox et al. "Formation of dense partonic matter in relativistic nucleus–nucleus collisions at RHIC: Experimental evaluation by the PHENIX Collaboration." In: *Nuclear Physics A* 757.1 (2005). First Three Years of Operation of RHIC, pp. 184–283. DOI: https://doi.org/10.1016/j.nuclphysa.2005.03.086.

[2] J. Adams et al. "Experimental and theoretical challenges in the search for the quark–gluon plasma: The STAR Collaboration's critical assessment of the evidence from RHIC collisions." In: *Nuclear Physics A* 757.1 (2005). First Three Years of Operation of RHIC, pp. 102–183. DOI: https://doi.org/10.1016/j.nuclphysa.2005.03.085.

[3] Wit Busza, Krishna Rajagopal, and Wilke van der Schee. "Heavy Ion Collisions: The Big Picture and the Big Questions." In: *Annual Review of Nuclear and Particle Science* 68.1 (2018), pp. 339–376. DOI: 10.1146/annurev-nucl-101917-020852.

[4] B. Abelev et al. "Centrality determination of Pb-Pb collisions at $\sqrt{s_{NN}} = 2.76$ TeV with ALICE." In: *Phys. Rev. C* 88 (4 2013), p. 044909. DOI: 10.1103/PhysRevC.88.044909.

[5] S. Chatrchyan et al. "Measurement of isolated photon production in pp and PbPb collisions at sNN=2.76 TeV." In: *Physics Letters B* 710.2 (2012), pp. 256–277. DOI: https://doi.org/10.1016/j.physletb.2012.02.077.

[6] Adam Olszewski and Wojciech Broniowski. "Partial correlation analysis method in ultrarelativistic heavy-ion collisions." In: *Phys. Rev. C* 96 (5 2017), p. 054903. DOI: 10.1103/PhysRevC.96.054903.

[7] B. B. Back et al. "Forward-backward multiplicity correlations in $\sqrt{s_{NN}} = 200$ GeV Au+Au collisions." In: *Phys. Rev. C* 74 (1 2006), p. 011901. DOI: 10.1103/PhysRevC.74.011901.

[8] B. I. Abelev et al. "Growth of Long Range Forward-Backward Multiplicity Correlations with Centrality in Au + Au Collisions at $\sqrt{s_{NN}} = 200$ GeV." In: *Phys. Rev. Lett.* 103 (17 2009), p. 172301. DOI: 10.1103/PhysRevLett.103.172301.

[9] M. Aaboud et al. "Measurement of forward-backward multiplicity correlations in lead-lead, proton-lead, and proton-proton collisions with the ATLAS detector." In: *Phys. Rev. C* 95 (6 2017), p. 064914. DOI: 10.1103/PhysRevC.95.064914.

[10] Jonah E. Bernhard et al. “Applying Bayesian parameter estimation to relativistic heavy-ion collisions: Simultaneous characterization of the initial state and quark-gluon plasma medium.” In: *Phys. Rev. C* 94 (2 2016), p. 024907. DOI: `10.1103/PhysRevC.94.024907`.

[11] Govert Nijs et al. “Bayesian analysis of heavy ion collisions with the heavy ion computational framework Trajectum.” In: *Phys. Rev. C* 103 (5 2021), p. 054909. DOI: `10.1103/PhysRevC.103.054909`.

[12] D. Everett et al. “Multisystem Bayesian constraints on the transport coefficients of QCD matter.” In: *Phys. Rev. C* 103 (5 2021), p. 054904. DOI: `10.1103/PhysRevC.103.054904`.

[13] M. Aaboud et al. “Fluctuations of anisotropic flow in Pb+Pb collisions at $\sqrt{s_{\text{NN}}} = 5.02$ TeV with the ATLAS detector.” In: *Journal of High Energy Physics* 2020.1 (2020). DOI: `10.1007/jhep01(2020)051`.

[14] Stefan Floerchinger, Eduardo Grossi, and Jorrit Lion. “Fluid dynamics of heavy ion collisions with mode expansion.” In: *Phys. Rev. C* 100 (1 2019), p. 014905. DOI: `10.1103/PhysRevC.100.014905`.

[15] M.L. Miller et al. “Glauber Modeling in High-Energy Nuclear Collisions.” In: *Annual Review of Nuclear and Particle Science* 57.1 (2007), pp. 205–243. DOI: `10.1146/annurev.nucl.57.090506.123020`.

[16] L. Adamczyk et al. “Azimuthal Anisotropy in $\mathrm{U}+\mathrm{U}$ and $\mathrm{Au}+\mathrm{Au}$ Collisions at RHIC.” In: *Phys. Rev. Lett.* 115 (22 2015), p. 222301. DOI: `10.1103/PhysRevLett.115.222301`.

[17] Wojciech Broniowski and Wojciech Florkowski. “Geometric relation between centrality and the impact parameter in relativistic heavy-ion collisions.” In: *Phys. Rev. C* 65 (2 2002), p. 024905. DOI: `10.1103/PhysRevC.65.024905`.

[18] Raimond Snellings. “Collective expansion at the LHC: selected ALICE anisotropic flow measurements.” In: *Journal of Physics G: Nuclear and Particle Physics* 41.12 (2014), p. 124007. DOI: `10.1088/0954-3899/41/12/124007`.

[19] “Improved version of the PHOBOS Glauber Monte Carlo.” In: *SoftwareX* 1-2 (2015), pp. 13 –18.

[20] Weiyao Ke et al. “Constraints on rapidity-dependent initial conditions from charged-particle pseudorapidity densities and two-particle correlations.” In: *Phys. Rev. C* 96 (4 2017), p. 044912. DOI: `10.1103/PhysRevC.96.044912`.

[21] J.S. Moreland, J.E. Bernhard, and S.A. Bass. "Alternative ansatz to wounded nucleon and binary collision scaling in high-energy nuclear collisions." In: *Phys. Rev. C* 92 (1 2015), p. 011901. DOI: 10.1103/PhysRevC.92.011901.

[22] Matthew Luzum. "Flow fluctuations and long-range correlations: elliptic flow and beyond." In: *Journal of Physics G: Nuclear and Particle Physics* 38.12 (2011), p. 124026. DOI: 10.1088/0954-3899/38/12/124026.

[23] K. H. Ackermann et al. "Elliptic Flow in $Au + Au$ Collisions at $\sqrt{s_{\mathrm{NN}}} = 130\mathrm{GeV}$." In: *Phys. Rev. Lett.* 86 (3 2001), pp. 402–407. DOI: 10.1103/PhysRevLett.86.402.

[24] Mingliang Zhou and Jiangyong Jia. "Centrality fluctuations in heavy-ion collisions." In: *Phys. Rev. C* 98 (4 2018), p. 044903. DOI: 10.1103/PhysRevC.98.044903.

[25] Jiangyong Jia, Chunjian Zhang, and Jun Xu. "Centrality fluctuations and decorrelations in heavy-ion collisions in a Glauber model." In: *Phys. Rev. Research* 2 (2 2020), p. 023319. DOI: 10.1103/PhysRevResearch.2.023319.

[26] Sruthy Jyothi Das et al. "Relating centrality to impact parameter in nucleus-nucleus collisions." In: *Phys. Rev. C* 97 (1 2018), p. 014905. DOI: 10.1103/PhysRevC.97.014905.

[27] Patrick Hanus, Klaus Reygers, and Aleksas Mazeliauskas. "Entropy production in pp and Pb-Pb collisions at energies available at the CERN Large Hadron Collider." In: *Phys. Rev. C* 100 (6 2019), p. 064903. DOI: 10.1103/PhysRevC.100.064903.

[28] Rudolph Rogly, Giuliano Giacalone, and Jean-Yves Ollitrault. "Reconstructing the impact parameter of proton-nucleus and nucleus-nucleus collisions." In: *Phys. Rev. C* 98 (2 2018), p. 024902. DOI: 10.1103/PhysRevC.98.024902.

[29] J. Adam et al. "Centrality Dependence of the Charged-Particle Multiplicity Density at Midrapidity in Pb-Pb Collisions at $\sqrt{s_{NN}} = 5.02$ TeV." In: *Phys. Rev. Lett.* 116 (22 2016), p. 222302. DOI: 10.1103/PhysRevLett.116.222302.

[30] J. Adam et al. "Centrality dependence of the pseudorapidity density distribution for charged particles in Pb–Pb collisions at $\sqrt{s_{NN}}$ =5.02 TeV." In: *Physics Letters B* 772 (2017), pp. 567–577. DOI: https://doi.org/10.1016/j.physletb.2017.07.017.

[31] S. Acharya et al. "Transverse momentum spectra and nuclear modification factors of charged particles in Xe–Xe collisions at $\sqrt{s_{NN}} = 5.44$ TeV." In: *Physics Letters B* 788 (2019), pp. 166–179. DOI: https://doi.org/10.1016/j.physletb.2018.10.052.

[32] Aleksas Mazeliauskas et al. "Fast resonance decays in nuclear collisions." In: *The European Physical Journal C* 79.3 (2019). DOI: 10.1140/epjc/s10052-019-6791-7.

[33] B. Abelev et al. “Centrality dependence of π, K, and p production in Pb-Pb collisions at $\sqrt{s_{NN}} = 2.76$ TeV.” In: *Phys. Rev. C* 88 (4 2013), p. 044910. DOI: 10.1103/PhysRevC.88.044910.

[34] C. Pruneau, S. Gavin, and S. Voloshin. “Methods for the study of particle production fluctuations.” In: *Phys. Rev. C* 66 (4 2002), p. 044904. DOI: 10.1103/PhysRevC.66.044904.

[35] S. Chatrchyan et al. “Studies of azimuthal dihadron correlations in ultra-central PbPb collisions at $\sqrt{s_{NN}}$=2.76 TeV.” In: *Journal of High Energy Physics* 2014.2 (2014). DOI: 10.1007/jhep02(2014)088.

[36] INDRA Collaboration et al. *Reconstructing the impact parameter dependence of experimental observables from intermediate energy heavy-ion collision data*. 2020. arXiv: 2011.04496 [nucl-ex].

[37] Petr Parfenov et al. “Relating Charged Particle Multiplicity to Impact Parameter in Heavy-Ion Collisions at NICA Energies.” In: *Particles* 4.2 (2021), pp. 275–287. DOI: 10.3390/particles4020024.

DECLARATION OF AUTHORSHIP

I hereby declare that I have written this Master Thesis by myself. I did not resort to any other sources than the ones listed in the bibliography.

Munich, July 2021

Kianusch Vahid Yousefnia